ACCEPTED MANUSCRIPT

The Journal of Chemical Physics

AIP Publishing

This is the author's peer reviewed, accepted manuscript. However, the online version of record will be different from this version once it has been copyedited and typeset.
PLEASE CITE THIS ARTICLE AS DOI:10.1063/1.5123013

The Static Local Field Correction of the Warm Dense Electron Gas: An *ab Initio* Path Integral Monte Carlo Study and Machine Learning Representation

T. Dornheim,[1, 2, *] J. Vorberger,[3] S. Groth,[2] N. Hoffmann,[3] Zh. A. Moldabekov,[4, 2] and M. Bonitz[2]

[1] *Center for Advanced Systems Understanding (CASUS), Görlitz, Germany*
[2] *Institut für Theoretische Physik und Astrophysik,*
Christian-Albrechts-Universität zu Kiel, Leibnizstraße 15, D-24098 Kiel, Germany
[3] *Helmholtz-Zentrum Dresden-Rossendorf, Bautzner Landstraße 400, D-01328 Dresden, Germany*
[4] *Institute for Experimental and Theoretical Physics,*
Al-Farabi Kazakh National University, Al-Farabi Str. 71, 050040 Almaty, Kazakhstan

The study of matter at extreme densities and temperatures as they occur in astrophysical objects and state-of-the art experiments with high-intensity lasers is of high current interest for many applications. While no overarching theory for this regime exists, accurate data for the density response of correlated electrons to an external perturbation are of paramount importance. In this context, the key quantity is given by the *local field correction* (LFC), which provides a wave-vector resolved description of exchange-correlation effects. In this work, we present extensive new path integral Monte Carlo (PIMC) results for the static LFC of the uniform electron gas, which are subsequently used to train a fully connected deep neural network. This allows us to present a representation of the LFC with respect to continuous wave-vectors, densities, and temperatures covering the entire warm dense matter regime. Both the PIMC data and neural-net results are available online. Moreover, we expect the presented combination of *ab initio* calculations with machine-learning methods to be a promising strategy for many applications.

I. INTRODUCTION

The uniform electron gas (UEG) [1, 2], often denoted as *jellium*, is one of the most fundamental model systems in quantum many-body theory. Having been originally introduced as a simple model for conduction electrons in metals [3], it offers a plethora of interesting physical phenomena such as Wigner crystallization [4–8], collective excitations [9–11], the possibility of a charge-/spin-density wave [12–15], and an incipient excitonic mode at low density [16–19]. Moreover, the accurate parametrization of its zero-temperature properties (e.g., Refs. [20–25]) based on ground-state quantum Monte Carlo (QMC) simulations [5, 26–30] has been pivotal for many applications, most notably as a basis for the striking success of density functional theory (DFT) regarding the description of real materials [31, 32].

Of particular importance is the response of the UEG to an external perturbation, which, within linear response theory, is fully captured by the density response function [33]

$$\chi(q,\omega) = \frac{\chi_0(q,\omega)}{1 - \frac{4\pi}{q^2}\left[1 - G(q,\omega)\right]\chi_0(q,\omega)} , \tag{1}$$

with q and ω being the respective wave number and frequency. Here $\chi_0(q,\omega)$ denotes the response function of the ideal (i.e., noninteracting) system, and the local field correction (LFC) $G(q,\omega)$ contains all *exchange-correlation* effects in χ [34, 35]. Consequently, finding an accurate theory for the LFC has been a long-standing problem for decades [34, 36]. Such information is crucial for many applications, including the interpretation of experiments [37–41], the construction of effective, electronically screened potentials [42–44], the development of advanced functionals for DFT [45–48], the incorporation of electronic correlations into quantum hydrodynamics [49–51], and the calculation of other material properties like electrical and thermal conductivities [52, 53], stopping power [54, 55], and energy transfer rates [56].

Consequently, a set of accurate data for the density response function and local field correction at zero temperature has been obtained on the basis of ground state-QMC simulations [27, 57, 58] in the static limit [i.e., $G(q,0) = G(q)$], which was subsequently used as input for the widespread analytical parametrization of $G(q)$ by Corradini *et al.* [59].

However, over the last years there has emerged a high interest in states of matter at extreme densities ($r_s = \bar{a}/a_\mathrm{B} \sim 1$, with $\bar{a}$ and a_B being the average particle distance and first Bohr radius) and temperatures ($\theta = k_\mathrm{B}T/E_\mathrm{F} \sim 1$, with E_F being the Fermi energy [2]) as it occurs in astrophysical objects like giant planet interiors [60–63] and brown dwarfs [64–66]. This so-called *warm dense matter* (WDM) can be realized and studied experimentally, e.g., via shock compression [67, 68], see Ref. [69] for a topical review article. Moreover, hot electrons have become important for many other communities, such as solid-state physics with laser excitations [70, 71], high-pressure physics [72], and hot-electron chemistry [73, 74]. Further, WDM is predicted to materialize on the pathway towards inertial confinement fusion [68, 75, 76] and is important for the study of radiation damage cascades in the walls of fission and fusion reactors [77]. Therefore, WDM has emerged as one of the most active frontiers in plasma physics and materials

---

[*] t.dornheim@hzdr.de

ACCEPTED MANUSCRIPT

The Journal of Chemical Physics

This is the author's peer reviewed, accepted manuscript. However, the online version of record will be different from this version once it has been copyedited and typeset.
PLEASE CITE THIS ARTICLE AS DOI:10.1063/1.5123013

AIP Publishing

science.

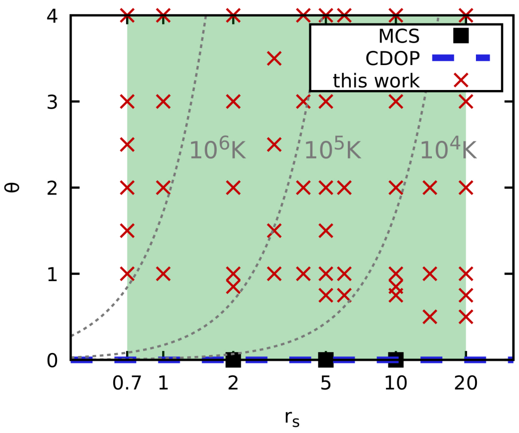

FIG. 1. Parameter overview of the r_s-θ plane: The dashed blue line depicts the ground state parametrization by Corradini *et al.* [59] (CDOP) and the black squares the diffusion Monte Carlo points from Ref. [27] (MCS) on which it is based. The red crosses correspond to our new PIMC data and the shaded green area depicts the parameter range for which our machine-learning representation (see Sec. III) has been constructed. The dotted grey curves indicate lines of constant temperature.

From a theoretical perspective, the intriguingly intricate interplay of 1) Coulomb coupling, 2) thermal excitations, and 3) quantum degeneracy effects prevents the application of perturbation expansions and renders the modelling of WDM a most formidable challenge [78]. In particular, the extension of ground state methods like DFT to these conditions [79, 80] requires accurate and readily available knowledge of the fundamental properties of electrons in the warm dense regime. This need has sparked a surge of new developments in the field of electronic QMC simulations at finite temperature [81–95], which recently culminated in the highly accurate parametrization of the exchange-correlation free energy of the UEG covering the entire WDM regime [96, 97], see Ref. [98] for a topical review article.

While being an important step in the right direction, a consistent and fundamental theory of WDM requires to go beyond the local density approximation [99, 100], with the electronic density response [see Eq. (1)] being of key importance. In this work, we aim to partly meet this demand by presenting a full description of the static local field correction $G(q;r_s,\theta)$ of the warm dense electron gas including all exchange-correlation effects. It is important to note that the results presented in this work correspond to the *exact static limit* of $G(q,\omega)$ and have not been obtained on the basis of a *static approximation* like many dielectric theories [101–103]. Moreover, we stress that $G(q)$ already constitutes a good approximation for $G(q,\omega)$ in many cases, as was recently demonstrated for the dynamic structure factor $S(q,\omega)$ in Refs. [18, 104].

In practice, we have carried out extensive path integral Monte Carlo (PIMC) simulations of the UEG at $N_\text{p}\sim 50$ density-temperature combinations in the range of $0.7\leq r_s\leq 20$ and $0.5\leq\theta\leq 4$, cf. the red crosses in Fig. 1. Here the main obstacle is given by the notorious fermion sign problem [105, 106], which prevents PIMC simulations below half the Fermi temperature and limits the feasible system size to $N=14,\dots,66$. The latter issue can be controlled by using a previously introduced finite-size correction [107], such that any remaining difference to the thermodynamic limit ($N\to\infty$) vanishes within the given accuracy. To overcome the restrictions regarding temperature, we combine our new PIMC data for $G(q)$ with the aforementioned ground-state parametrization (dashed blue line in Fig. 1) based on the zero-temperature QMC data by Moroni *et al.* [27] (black squares). These combined data are then used to *train* a fully-connected deep neural net [108], which smoothly interpolates our data grid and provides accurate results for $G(q;r_s,\theta)$ at continuous densities and temperatures (see the green area in Fig. 1) for up to five times the Fermi wave number, $0\leq q\leq 5q_\text{F}$.

Both the new, machine-learning based representation of the static LFC and the extensive PIMC raw data have been made freely available online [111], and can be used directly for the applications listed in the beginning. Moreover, the investigation both of the density response function $\chi(q)$ and $G(q)$ itself are interesting in their own right, and we find a pronounced dependence of the LFC on density and temperature, with a nontrivial behaviour around intermediate q-values and a negative large-q tail for certain parameters. Furthermore, our results can be used to comprehensively gauge the accuracy of widely used approximations like dielectric theory [101–103, 112] and to benchmark and guide the developments of new methods [113]. Finally, we expect the presented combination of computationally expensive *ab initio* calculations with modern machine-learning methods to be a promising strategy for many applications in many-body physics and beyond.

The paper is organized as follows: In Sec. II, we introduce our *ab initio* PIMC approach to compute the density response function $\chi(q)$, which allows to subsequently extract the desired local field correction. Moreover, we briefly discuss finite-size effects in our PIMC data, and demonstrate how they can be effectively removed. Sec. III is devoted to the machine-learning representation of $G(q;r_s,\theta)$, including discussions of the selected parameter range (III A) and the observed nontrivial behavior of G with respect to density and temperature (III B). Finally, we briefly summarize our results and motivate their utility for future applications (IV).

II. PIMC APPROACH TO THE STATIC DENSITY RESPONSE

We use a canonical adaption [114, 115] of the worm algorithm by Boninsegni *et al.* [116, 117] to carry out PIMC

The Journal of Chemical Physics
ACCEPTED MANUSCRIPT
This is the author's peer reviewed, accepted manuscript. However, the online version of record will be different from this version once it has been copyedited and typeset.
PLEASE CITE THIS ARTICLE AS DOI:10.1063/1.5123013
AIP Publishing

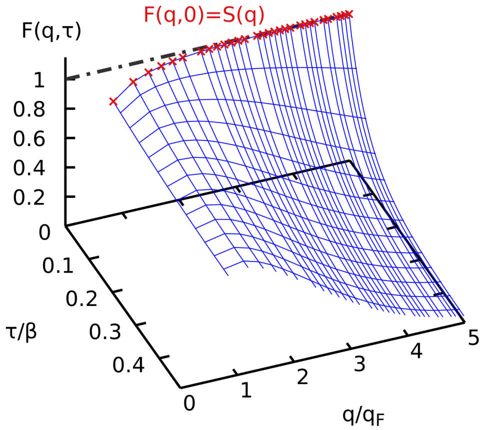

FIG. 2. PIMC results for the imaginary-time density-density correlation function $F(q,\tau)$ for $N = 14$ unpolarized electrons at $r_s = 1$ and $\theta = 2$. For $\tau = 0$, it is equal to the static structure factor $S(q)$.

simulations of $N = 2N_\uparrow = 2N_\downarrow$ unpolarized electrons in a volume V at a reduced temperature θ. A detailed introduction of the PIMC method has been presented elsewhere [98, 118]. Further, we stress that we do not impose any nodal restrictions [119], and our results are exact within the given Monte Carlo error bars.

Of particular importance in the context of the present work is the imaginary-time density correlation function F (see Ref. [104] for details), which is defined as

$$F(q,\tau) = \frac{1}{N}\left\langle \rho(q,\tau)\rho(-q,0)\right\rangle \ , \tag{2}$$

with $\rho(q,\tau)$ being the density operator. In Fig. 2, we show PIMC results for Eq. (2) for $N = 14$ electrons at $r_s = 1$ and $\theta = 2$ over the q-τ-plane. Since a direct physical interpretation of $F(q,\tau)$ is rather difficult, here we only mention that it approaches the static structure factor $S(q)$ in the limit $\tau = 0$ and that it is symmetric with respect to $\tau = \beta/2$ ($\beta = 1/k_\mathrm{B}T$). The depicted q-grid is a direct consequence of the momentum quantization in a finite simulation cell, whereas the τ-grid can, in principle, be made arbitrarily fine. We also note that $F(q,\tau)$ is connected to the dynamic structure factor $S(q,\omega)$ via a Laplace transform, which can be used as a starting point for the reconstruction of dynamic properties, see Refs. [18, 104].

The main utility of F in this work is the imaginary-time analogue of the fluctuation–dissipation theorem, which states that the static density response function can be computed as a simple one-dimensional integral along the τ-axis [120, 121],

$$\chi(q) = -n \int_0^\beta \mathrm{d}\tau\ F(q,\tau) \quad . \tag{3}$$

The results for Eq. (3) are shown in Fig. 3 again for $r_s = 1$ and $\theta = 2$ as the red crosses for $N = 14$. As a reference, we also include the widely used random phase approximation (RPA, dashed blue), which is obtained by setting $G(q,\omega) = 0$ in Eq. (1). This mean-field description of the static density response function is exact in the limits of $q \to 0$ and $q \to \infty$, but significantly deviates in between. Furthermore, the solid green line corresponds to the ideal response function $\chi_0(q)$, which becomes exact for large q, but does not entail the screening effects that are manifest in the PIMC and RPA curves for small q [122].

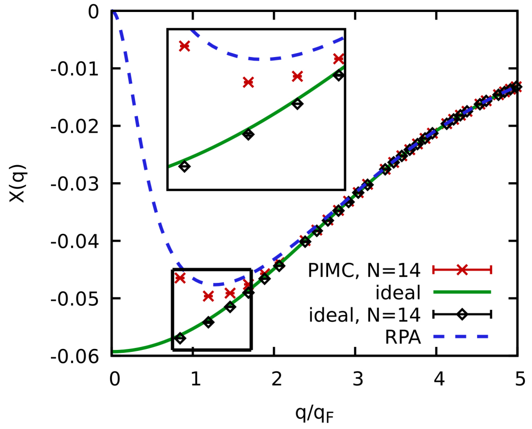

FIG. 3. Wave-number dependence of the static density response function $\chi(q)$ for $r_s = 1$ and $\theta = 2$. The red crosses show PIMC results for $N = 14$ computed as an integral over $F(q,\tau)$ [cf. Eq. (2)] and the black diamonds the ideal response function for the same N obtained from Configuration PIMC [107]. The solid green and dashed blue lines correspond to $\chi_0(q)$ and $\chi_\mathrm{RPA}(q)$ in the TDL.

The primary objective of this paper is the computation of the static LFC, which can be obtained from $\chi(q)$ by solving Eq. (1) for $G(q)$, i.e.,

$$G(q) = 1 - \frac{q^2}{4\pi}\left(\frac{1}{\chi_0(q)} - \frac{1}{\chi(q)}\right) \ . \tag{4}$$

The results for Eq. (4) are shown in Fig. 4 a) for the same conditions as in Figs. 2 and 3 for three different particle numbers. First and foremost, we note that the error bars increase for large q. This is a direct consequence of the definition of $G(q)$ as a deviation measure between $\chi(q)$ and $\chi_0(q)$, cf. Eq. (4), which can be understood as follows: for small q, both functions are significantly different, and $G(q)$ can be accurately resolved. In contrast, they converge for large q and the small remaining deviation is enhanced by the $q^2/4\pi$ pre-factor, which results in an increasing statistical uncertainty in the LFC. In practice, this means that we get accurate data for $G(q)$ when it has an important impact on the density response, whereas our estimation gets worse when $\chi(q)$ is essentially equal to the noninteracting response function in the first place.

The Journal of Chemical Physics
ACCEPTED MANUSCRIPT
This is the author's peer reviewed, accepted manuscript. However, the online version of record will be different from this version once it has been copyedited and typeset.
PLEASE CITE THIS ARTICLE AS DOI:10.1063/1.5123013

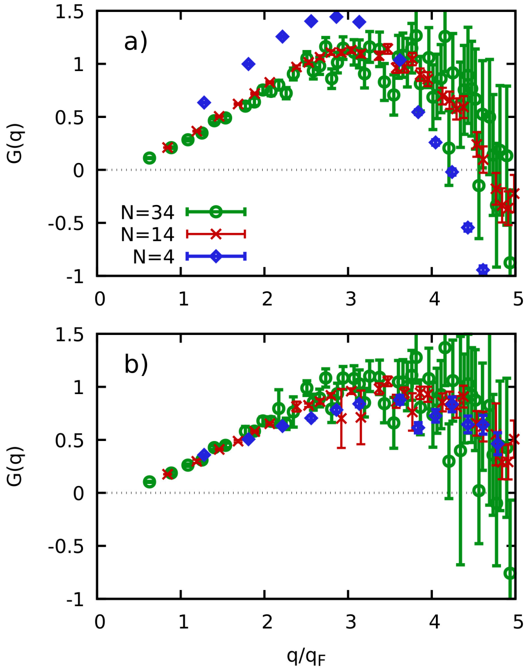

FIG. 4. Extracting the static local field correction: Panel a) shows PIMC data for $G(q)$ for $r_s = 1$ and $\theta = 2$ for $N = 34$ (green circles), $N = 14$ (red crosses), and $N = 4$ (blue diamonds) unpolarized electrons computed from Eq. (4) using $\chi(q)$. Panel b) shows the same data after the finite-size correction using $\chi_0^N(q)$.

Secondly, there are significant finite-size effects, which are particularly pronounced for $N = 4$ (blue diamonds) as it is expected. The origin of this N-dependence in our PIMC data has been extensively discussed by Groth *et al.* [107], and is given by the system-size dependence of the ideal response function. This is illustrated by the black diamonds in Fig. 3, which depict configuration PIMC data for $\chi_0(q)$ for $N = 14$ ideal fermions. While the deviations to the green curve are small, they do indeed become particularly significant when χ and χ_0 converge. Since we are ultimately interested in a description of $G(q)$ in the thermodynamic limit, we finite-size correct our results by substituting the size-consistent ideal response function χ_0^N (which we computed using configuration PIMC, see Ref. [107]) for χ_0 in Eq. (4), and the results are shown in Fig. 4 b). Evidently, the system-size dependence has been drastically reduced even for as few as $N = 4$ electrons, and the curves for $N = 14$ and $N = 34$ cannot be distinguished within the error bars. For completeness, we mention that the increased error bars at $N = 34$ are a direct consequence of the fermion sign problem, see Ref. [105] for an extensive discussion.

This procedure has been applied to all PIMC data shown in this work. For completeness, we mention that a PIMC simulation for a single r_s-θ-combination takes $\mathcal{O}\left(10^3\right) - \mathcal{O}\left(10^4\right)$ CPU (single-core) hours, which are carried out in parallel on a cluster.

III. REPRESENTATION OF THE STATIC LOCAL FIELD CORRECTION

The ultimate goal of this work is the construction of a representation of the static local field correction with respect to continuous wave numbers, densities, and temperatures, $G(q; r_s, \theta)$. To this end, we have repeated the workflow introduced in Sec. II for $N_\mathrm{p} \sim 50$ different density-temperature combinations, and, to exclude the possibility of finite-size effects, often for different particle numbers N.

A. Parameter range

Let us first discuss the available range of wave numbers q. Due to the aforementioned momentum quantization in a finite simulation cell, PIMC data are only available down to a minimum value of $q_\mathrm{min} = 2\pi/L$, with $L = V^{1/3}$ being the box length. This, however, does not constitute a problem since the exact $q \to 0$ limit is known from the compressibility sum-rule, which states that [102]

$$\lim_{q\to 0} G(q) = -\frac{q^2}{4\pi}\frac{\partial}{\partial n^2}\left(n f_\mathrm{xc}\right) \ , \tag{5}$$

with n being the density. In practice, Eq. (5) is evaluated using the accurate parametrization of the exchange-correlation free energy f_xc from Ref. [96].

The large-q behaviour, on the other hand, is more difficult. As explained in Sec. II, the relative uncertainty of our PIMC data increases with q, and $q = 5q_\mathrm{F}$ does constitute a practical limit in many cases. Furthermore, the exact asymptotic expression for $q \to \infty$ introduced by Holas [123] only holds for $\theta = 0$ and must not simply be extended to finite temperature [124]. Therefore, we presently restrict ourselves to the range $0 \leq q \leq 5q_\mathrm{F}$, which is fully sufficient for all practical applications [125].

The second relevant parameter range is the reduced temperature θ. Since 1) the effect of $G(q)$ on $\chi(q)$ vanishes for large θ and 2) $G(q)$ eventually approaches the classical limit for any finite q, $\theta_\mathrm{max} = 4$ constitutes a reasonable limit for WDM research. In addition, it is clear that a useful representation of $G(q; r_s, \theta)$ should extend down to the ground state. In this regard, we have chosen to incorporate the ground-state parametrization from Ref. [59], which is based on QMC data [27] for $r_s = 2, 5$, and 10, cf. Fig. 1. Still, we note that CDOP is expected to be reasonably accurate both for larger and smaller densities, since it included the exact limit for small and large q-values for all r_s. Therefore, the validity range of our results regarding temperature is given by $0 \leq \theta \leq 4$.

The last parameter range to be selected is the density parameter r_s. For small r_s (i.e., high density), the system becomes weakly coupled. Hence, the influence of the local field correction vanishes and the RPA already provides an accurate description of the density response [35]. In practice, we choose $r_s = 0.7$ as the high-density limit of our representation, as it roughly coincides with core

The Journal of Chemical Physics ACCEPTED MANUSCRIPT

This is the author's peer reviewed, accepted manuscript. However, the online version of record will be different from this version once it has been copyedited and typeset.
PLEASE CITE THIS ARTICLE AS DOI:10.1063/1.5123013

AIP Publishing

densities of giant planets [64]. Upon increasing r_s, the system becomes sparser and approaches a strongly coupled electron liquid. While this regime does not pose a challenge for our PIMC simulations, the selected range of $0.7 \leq r_s \leq 20$ is fully sufficient for WDM applications.

B. Physical behavior and neural net representation

In the ground state, the static local field correction is relatively weakly dependent on r_s and both the large- and small-q limits are known analytically. Therefore, fitting an analytical representation to a QMC data set is a good strategy to obtain a smooth representation with only little bias [27, 59]. This situation, however, drastically changes at finite temperature. This can be seen in Fig. 5, where we show G in the q-θ-plane for three different values of the density parameter r_s.

At zero-temperature, the LFC is of a parabolic form at small q [cf. Eq. (5)], exhibits a saddle point around $q \approx 3q_\mathrm{F}$, and finally reaches the asymptotic limit predicted by Holas [123]. In particular, it holds

$$\lim_{q\to\infty} G(q;r_s,0) = B(r_s) + C(r_s)q^2 \ , \qquad (6)$$

where the constants B and C have been parametrized in Ref. [27]. More specifically, the pre-factor C is directly proportional to the change in the kinetic energy due to exchange-correlation effects [27, 123, 126]. Hence, C is positive for all r_s, and $G(q)$ exhibits a positive tail at $\theta = 0$.

At finite temperature, on the other hand, $G(q)$ behaves entirely different. At strong coupling (e.g., $r_s = 10$, panel a) and high temperature, the UEG converges towards the classical one-component plasma and $G(q)$ becomes flat. This can be understood heuristically from Eq. (6) in the following way: for the classical system, the kinetic energy per particle attains the ideal value $K_\mathrm{cl} = 3k_\mathrm{B}T/2$, and the pre-factor C vanishes. Therefore, while Eq. (6) quantitatively holds only for $\theta = 0$, it still predicts the correct qualitative behavior for $\theta > 0$ in this case. Moreover, we note that our PIMC data for $G(q)$ at $r_s = 10$ exhibit a small yet significant maximum at around $q \approx 3q_\mathrm{F}$ followed by a minimum depending on temperature.

At $r_s = 5$ and $r_s = 2$, which are located in the warm dense matter regime, the situation becomes even more complicated and, thus, interesting. While the large-q behavior of $G(q)$ eventually always becomes flat for high temperature (for every finite value of q), and approaches Eq. (6) towards $\theta = 0$, we observe *negative tails* in the vicinity of the Fermi temperature. This can be seen even more clearly in Fig. 6, where we show $G(q;r_s,\theta)$ in the r_s-q-plane. Panel a) corresponds to $\theta = 4$ and exhibits the expected classical, flat behavior at large q. Panel b) depicts results for the Fermi temperature, and nicely illustrates the pronounced r_s-dependence of G in the warm dense matter regime: at large r_s, $G(q)$ exhibits the by now familiar structure with a maximum, minimum, and a positive tail. With increasing density, the minimum becomes less distinct and eventually vanishes as the large-momentum tail becomes negative, and it clearly holds $G(q) < 0$.

To understand this nontrivial finding, we might again consider Eq. (6), which predicts that the tail is parabolic

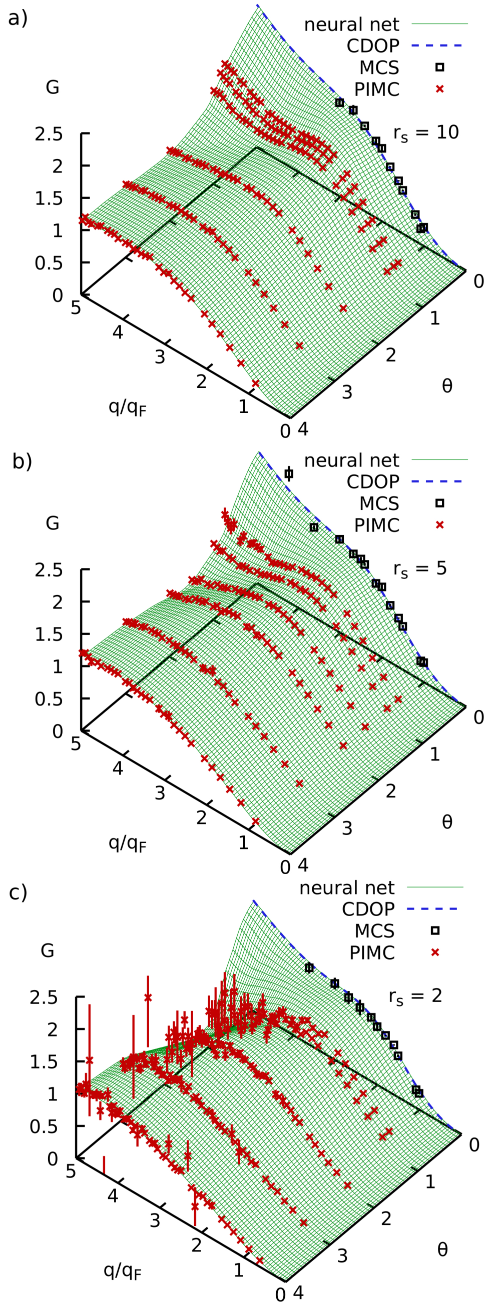

FIG. 5. The static local field correction in the temperature-wave number plane for a) $r_s = 10$, b) $r_s = 5$, and c) $r_s = 2$: The dashed blue line depicts the ground state parametrization by Corradini *et al.* [59] and the black squares the diffusion Monte Carlo points from Ref. [27] on which it is based. The red crosses correspond to our new PIMC data computed from Eq. (3), and the green surface shows the machine-learning prediction.

The Journal of Chemical Physics
ACCEPTED MANUSCRIPT
This is the author's peer reviewed, accepted manuscript. However, the online version of record will be different from this version once it has been copyedited and typeset.
PLEASE CITE THIS ARTICLE AS DOI:10.1063/1.5123013
AIP Publishing

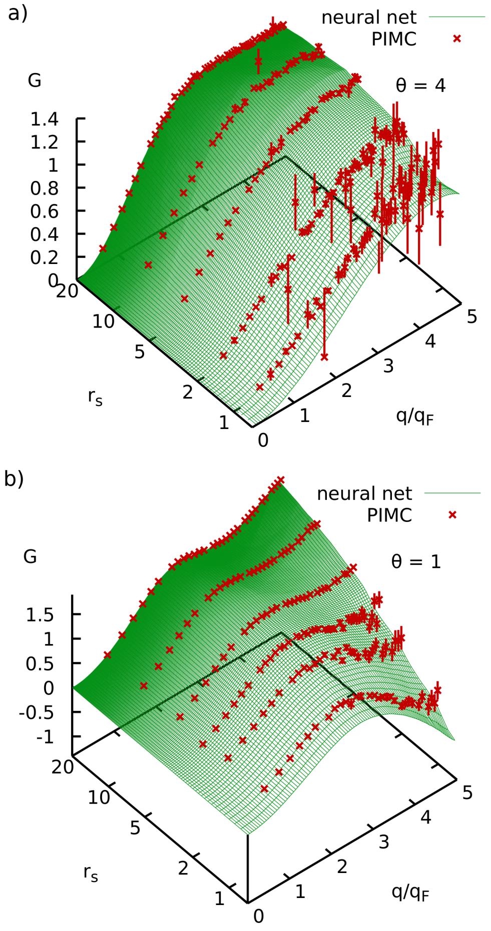

FIG. 6. The static local field correction in the r_s-wave number plane for a) $\theta = 4$ and b) $\theta = 1$: The red crosses correspond to our new PIMC data computed from Eq. (3), and the green surface shows the machine-learning prediction.

with $K_{\rm xc} = K - K_0$ being the pre-factor. It has been known for some time [127, 128] that $K_{\rm xc}$ of the UEG does indeed become negative precisely in the WDM regime. While we again stress that the derivation of Eq. (6) is not valid at $\theta > 0$ and that it does not quantitatively agree with our PIMC data, it is still likely that the change of the sign in $K_{\rm xc}$ is directly connected to the observed nontrivial behavior in $G(q; r_s, \theta)$.

In summary, we have found that the LFC does exhibit a distinct dependence on density and temperature, for which, despite being qualitatively understood, no analytical formula exists. Therefore, the utilization of an analytical fit formula would most likely introduce an artificial bias. In contrast, modern machine-learning methods provide a flexible alternative in this situation and have emerged as a powerful tool for universal function approximation [129, 130] that is not afflicted with this shortcoming. In particular, we have used our extensive set of PIMC and CDOP data [cf. Fig. 1] to train a fully-connected deep neural network (see Appendix A for details), which can then be used to predict $G(q; r_s, \theta)$ at continuous values of all three parameters in the specified parameter range.

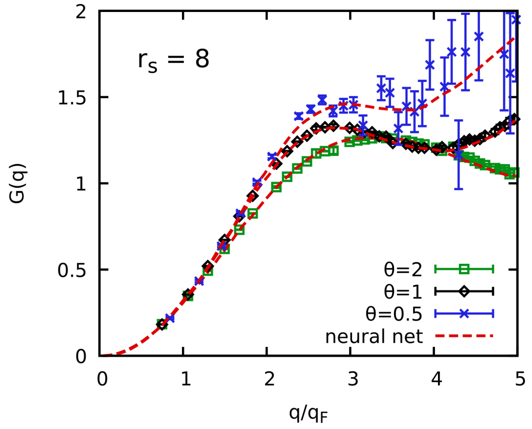

FIG. 7. Validation of the machine-learning representation: Shown is the wave-number dependence of $G(q)$ for three different temperatures at $r_s = 8$. The different symbols correspond to finite-size corrected PIMC data that have not been included in the training of the neural net (cf. Fig. 1), and the red curves to the machine-learning prediction.

The results of this procedure are shown as the green surfaces in Figs. 5 and 6. First and foremost, we note the excellent agreement with the input data over the entire parameter range. More specifically, we find a mean deviation measure of

$$\chi = \frac{1}{N_{\rm data}} \sum_{k=1}^{N_{\rm data}} |G^k_{\rm nn} - G^k_{\rm PIMC}| \approx 0.03 \quad . \qquad (7)$$

In addition, the utilized weight regularization (cf. Appendix A) brings about smooth curves with little generalisation errors, even in the most uncertain range of $0 < \theta < 0.5$.

In Fig. 7, we compare independent PIMC data for $r_s = 8$ and three different temperatures that have not been included into the training of the neural net with the corresponding machine-learning prediction to validate the learned representation. The PIMC data for $\theta = 2$ (green squares) and $\theta = 1$ (black diamonds) are of high quality, and are in remarkable agreement with the neural net (red curves). At $\theta = 0.5$, the simulations are computationally expensive due to the fermion sign problem (we find an average sign of $S \approx 0.01$, see Ref. [105] for an extensive discussion) and the statistical uncertainty is substantial for large q. Still, the neural net is capable to provide a prediction that is fully consistent with the benchmark data even in a regime where the training data are sparse.

The Journal of Chemical Physics ACCEPTED MANUSCRIPT

This is the author's peer reviewed, accepted manuscript. However, the online version of record will be different from this version once it has been copyedited and typeset.
PLEASE CITE THIS ARTICLE AS DOI:10.1063/1.5123013

AIP Publishing

IV. SUMMARY AND OUTLOOK

In this paper, we have presented extensive new PIMC results for the static local field correction $G(q)$ of the warm dense electron gas for $N_\mathrm{p} \sim 50$ different density-temperature combinations and different particle numbers. These data—together with the ground-state parametrization from Ref. [59]—have subsequently been used as input to train a fully-connected deep neural network to learn the function $G(q; r_s, \theta)$. This has allowed us to obtain a fast, reliable, and continuous representation of the LFC covering the entire warm dense matter regime. More specifically, we avoid any artificial bias due to an insufficient analytical representation (only few exact properties of $G(q; r_s, \theta)$ are known analytically at finite θ) and have carefully validated the machine-learning prediction against independent benchmark data.

In addition to the expected utility of our results for future applications (see below), the investigation of $G(q; r_s, \theta)$ is interesting in its own right, and we find a nontrivial and distinct dependence on density, temperature and wave number. In particular, $G(q)$ does exhibit a *negative tail* at large q in the vicinity of the Fermi temperature, which can most likely be attributed to a change in the sign of the exchange-correlation part of the kinetic energy.

We are confident that the presented full description of $G(q; r_s, \theta)$ will open up new avenues for many research applications. First and foremost, our representation can directly be used to study interesting properties of the UEG itself, like the possibility of a charge-density wave [12–14] and instabilities [17]. Further, G gives direct access to other important properties like the density-response function $\chi(q)$ [cf. Eq. (1)] and the static dielectric function $\epsilon(q)$. In addition, both our data and the neural net can be used to benchmark the accuracy of widespread approximations from dielectric theory like STLS [101, 102] and its recent improvement by Tanaka [103], and to guide the development of new approaches [113].

While the present study of the LFC is restricted to the static limit, it has recently been shown that, even without taking the frequency dependence of $G(q, \omega)$ into account, many dynamical properties can be accurately estimated [18, 104]. For example, our representation of $G(q; r_s, \theta)$ can be directly used to compute the electronic dynamic structure factor $S(q, \omega)$ in a static approximation, which fully captures both the negative dispersion relation and the correlation induced broadening of the spectra due to exchange-correlation effects. Such readily available, yet accurate predictions of $S(q, \omega)$ are very valuable in many fields, most notably the interpretation of scattering experiments [37, 131], which have emerged as a standard method of diagnostics in WDM experiments.

Moreover, we mention the utility of $G(q; r_s, \theta)$ as input for other simulations like quantum hydrodynamics [49–51], the construction of effective potentials [42–44], and for the computation of other material properties like electrical and thermal conductivities [52, 53]. Furthermore, our results can be used to construct advanced functionals for DFT based on the adiabatic-connection fluctuation-dissipation formalism [45–48], or as the basis for the exchange-correlation kernel in time-dependent DFT [132].

Lastly, we are convinced that the strategy to use machine-learning methods as a continuous representation of computationally expensive quantum Monte Carlo data is not limited to the present application, and can be further developed as a powerful paradigm in warm dense matter theory and beyond.

Both our extensive set of PIMC data and the machine-learning representation have been made freely available online [111].

ACKNOWLEDGMENTS

We gratefully acknowledge valuable feedback by M. Bussmann. In addition, we thank T. Sjostrom and S. Tanaka for sending us the VS and HNC data shown in Fig. 11. This work has been partially supported by the Deutsche Forschungsgemeinschaft via project BO1366/13, by the Ministry of Education and Science of the Republic of Kazakhstan (MES RK) under grant no. BR05236730, and by the Center of Advanced Systems Understanding (CASUS) which is financed by Germany's Federal Ministry of Education and Research (BMBF) and by the Saxon Ministry for Science and Art (SMWK) with tax funds on the basis of the budget approved by the Saxon State Parliament. We further acknowledge CPU time at the Norddeutscher Verbund für Hoch- und Höchleistungsrechnen (HLRN) via grant shp00015, at the clusters *hypnos* and *hemera* at Helmholtz-Zentrum Dresden-Rossendorf (HZDR), and at the computing centre of Kiel university.

Appendix A: Neural net training and layout

To generate the training data for the neural network, we construct cubic basis splines $G_\mathrm{s}^{r_s,\theta}(q)$ connecting Eq. (5) at small q with our PIMC data for $q \geq 2\pi/L$. To prevent overfitting of the statistical noise, the smoothness of the splines $G_\mathrm{s}(q)$ is chosen such that

$$\chi_w = \frac{1}{M}\sum_{i=1}^{M} \frac{\left|G^{r_s,\theta}(q_i) - G_\mathrm{s}^{r_s,\theta}(q_i)\right|}{\Delta G^{r_s,\theta}(q_i)} \geq 0.9 \ , \quad \text{(A1)}$$

with the M input points containing both PIMC and CSR data. This is illustrated in Fig. 8 for $r_s = 3$ and $\theta = 1$, with the spline (solid black) smoothly interpolating the somewhat noisy PIMC data (green crosses) and reproducing the CSR for small q (blue diamonds). This procedure has three main advantages: 1) evaluating the already smoothed spline to generate the training

ACCEPTED MANUSCRIPT

The Journal of Chemical Physics

This is the author's peer reviewed, accepted manuscript. However, the online version of record will be different from this version once it has been copyedited and typeset.

PLEASE CITE THIS ARTICLE AS DOI:10.1063/1.5123013

AIP Publishing

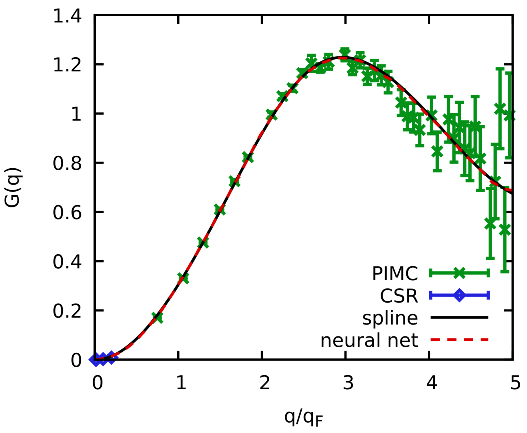

FIG. 8. Generation of the ML-input for $G(q; r_s, \theta)$ for $r_s = 3$ and $\theta = 1$. Shown are the finite-size corrected PIMC data (green crosses), points from the CSR [c.f. Eq. (5), blue diamonds] for small q, and a cubic basis spline (solid black). In addition, the dashed red line corresponds to the curve learned by the neural net.

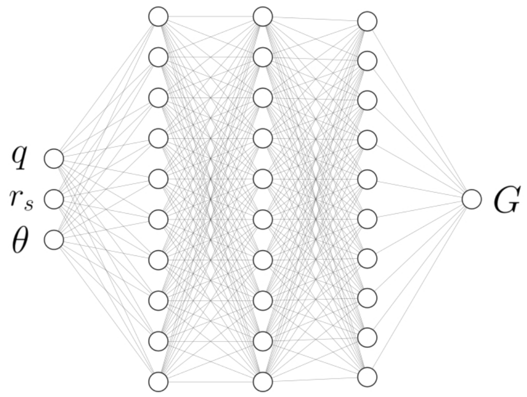

FIG. 9. Schematic illustration of the machine-learning representation of the static local field correction $G(q; r_s, \theta)$. The first layer is comprised of three neurons corresponding to the function arguments q, r_s, and θ, and the final layer gives the prediction for $G(q; r_s, \theta)$. The net is fully connected and contains $N_\mathrm{l} = 40$ hidden layers with $N_\mathrm{n} = 64$ neurons each.

data makes the training of the net more stable, 2) it allows us to generate the training data on an equidistant q-grid, whereas the PIMC raw data become denser for large q, which could potentially bias the quality of the net, and 3) it stabilizes the net in the small intermediate q-range where neither PIMC nor CSR data are available (cf. Fig. 8).

In addition, we include CDOP [59] data at $\theta = 0$ for $r_s = 0.7, 1, 2, 3, 4, 5, 6, 10, 14, 20$ into our training set. The total number of $G(q; r_s, \theta)$ samples is given by $N_\mathrm{train} \sim 6.5 \times 10^4$.

In Fig. 9, we show a schematic illustration of the fully connected deep neural network representing the static LFC [108]. The first layer corresponds to the three input variables q, r_s, and θ, and the final layer provides the desired prediction of $G(q; r_s, \theta)$. Moreover, there are $N_\mathrm{l} = 40$ hidden layers with $N_\mathrm{n} = 64$ neurons each. This combination was found empirically and is sufficiently flexible to accommodate the complicated behavior of $G(q; r_s, \theta)$. In addition, we note that fully connected networks are particularly powerful regarding function approximation [129]. We choose to optimize the neural network by ADAM [133] and fixed its parameters to $\beta_1 = 0.9$, $\beta_2 = 0.999$, and learning rate $\lambda = 0.001$. Furthermore, we reduced the generalization error by layer-wise L2 regularization of weights (excluding bias) at 6×10^{-7}.

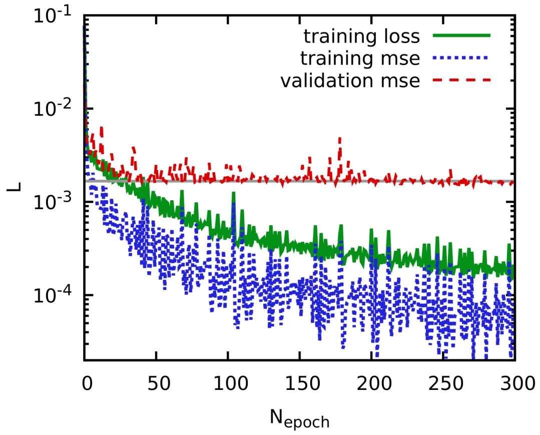

FIG. 10. Convergence of the training. The dotted blue and solid green lines show the mean-squared-error (mse) and the loss function (mse and weight regularization) as a function of the number of epochs. The dashed red line corresponds to the mse with respect to independent validation data ($[r_s = 1.25, \theta = 1.5]$,$[r_s = 8, \theta = 0.5, 0.75, 1.0, 2.0]$, $[r_s = 0.85, \theta = 1.5]$, and $[r_s = 4, \theta = 1.5]$), and the solid grey line to a constant fit for $200 \leq N_\mathrm{epoch} \leq 300$.

Finally, the convergence behavior of the training is illustrated in Fig. 10. The dotted blue line corresponds to the mean-squared-error (mse) with respect to the training data, and the solid green line to the actual loss function, which consists of both mse and the aforementioned weight-regularization. Therefore, the loss function is always larger than the pure mse. In addition, the red dashed line shows the mse computed with respect to independent validation data ($N_\mathrm{v} \sim 8 \times 10^3$ samples for $G(q; r_s, \theta)$, see the caption of Fig. 10) that were not included in the training. The solid grey line shows the average of the validation mse computed for $200 \leq N_\mathrm{epoch} \leq 300$, where the latter remains almost constant. This strongly implies the absence of a generalization error in our training procedure.

The Journal of Chemical Physics
ACCEPTED MANUSCRIPT
AIP Publishing
This is the author's peer reviewed, accepted manuscript. However, the online version of record will be different from this version once it has been copyedited and typeset.
PLEASE CITE THIS ARTICLE AS DOI:10.1063/1.5123013

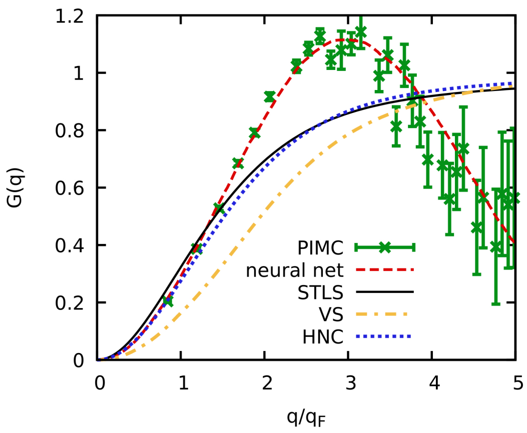

FIG. 11. Wave-number dependence of the static local field correction at $r_s = 2$ and $\theta = 1$. The green crosses and dashed red line correspond to our new finite-size corrected PIMC data and the machine-learning representation. In addition, we show several dielectric approximations, namely Singwi-Tosi-Land-Sjölander [101] (STLS, solid black), Vashista-Singwi [102] (VS, dash-dotted yellow), and the recent hypernetted-chain based approach by Tanaka [103] (HNC, dotted blue).

Appendix B: Comparison to dielectric theory

In Fig. 11, we compare our PIMC data (green crosses) and machine-learning representation (dashed red line) to various dielectric approximations for $r_s = 2$ and $\theta = 1$, i.e., at the center of the WDM regime. While the recent hypernetted-chain based approach by Tanaka [103] constitutes a remarkable improvement over STLS [101] (solid black), and Vashista-Singwi [102] (dash-dotted yellow) at small q, no approximation is capable to qualitatively reproduce the full nontrivial behavior of $G(q)$ at these conditions. Therefore, the new *ab initio* data presented in this work are indispensable to achieve a more fundamental understanding of the electronic density response.

A more detailed benchmark study of dielectric theory is beyond the scope of this work and will be presented elsewhere.

REFERENCES

[1] P.-F. Loos and P.M.W. Gill, The uniform electron gas, *Comput. Mol. Sci.* **6**, 410-429 (2016)

[2] G. Giuliani and G. Vignale, Quantum Theory of the Electron Liquid, Cambridge University Press (2008)

[3] G.D. Mahan, Many-Particle Physics, Springer Science+Business Media, New York (2000)

[4] E. Wigner, On the interaction of electrons in metals, *Phys. Rev.* **46**, 1002 (1934)

[5] D.M. Ceperley and B.J. Alder, Ground State of the Electron Gas by a Stochastic Method, *Phys. Rev. Lett.* **45**, 566 (1980)

[6] N.D. Drummond, Z. Radnai, J.R. Trail, M.D. Towler, and R.J. Needs, Diffusion quantum Monte Carlo study of three-dimensional Wigner crystals, *Phys. Rev. B* **69**, 085116 (2004)

[7] K. Utsumi and S. Ichimaru, Dielectric formulation of strongly coupled electron liquids at metallic densities. IV. Static properties in the low-density domain and the Wigner crystallization, *Phys. Rev. B* **24**, 3220 (1981)

[8] J.R. Trail, M.D. Towler, and R.J. Needs, *Phys. Rev. B* **68**, 045107 (2003)

[9] D. Pines and P. Nozieres, Theory of Quantum Liquids, CRC Press, Boca Raton, Florida, USA (2018)

[10] D. Pines and D. Bohm, A Collective Description of Electron Interactions: II. Collective vs Individual Particle Aspects of the Interactions, *Phys. Rev.* **85**, 338 (1952)

[11] D. Bohm and D. Pines, A Collective Description of Electron Interactions: III. Coulomb Interactions in a Degenerate Electron Gas, *Phys. Rev.* **92**, 609 (1953)

[12] H. Iyetomi, K. Utsumi, and S. Ichimaru, Dielectric formulation of strongly coupled electron liquids at metallic densities. V. Possibility of a charge-density-wave instability, *Phys. Rev. B* **24**, 3226 (1981)

[13] A. Holas and S. Rahman, Dynamic local-field factor of an electron liquid in the quantum versions of the Singwi-Tosi-Land-Sjl̈ander and Vashishta-Singwi theories, *Phys. Rev. B* **35**, 2720 (1987)

[14] H.K. Schweng and H.M. Böhm, Finite-temperature electron correlations in the framework of a dynamic local-field correction, *Phys. Rev. B* **48**, 2037 (1993)

[15] A.W. Overhauser, Spin Density Waves in an Electron Gas, *Phys. Rev.* **128**, 1437 (1962)

[16] Y. Takada and H. Yasuhara, Dynamical Structure Factor of the Homogeneous Electron Liquid: Its Accurate Shape and the Interpretation of Experiments on Aluminum, *Phys. Rev. Lett.* **89**, 216402 (2002)

[17] Y. Takada, Emergence of an excitonic collective mode in the dilute electron gas, *Phys. Rev. B* **94**, 245106 (2016)

[18] T. Dornheim, S. Groth, J. Vorberger, and M. Bonitz, *Ab initio* Path Integral Monte Carlo Results for the

The Journal of Chemical Physics ACCEPTED MANUSCRIPT

This is the author's peer reviewed, accepted manuscript. However, the online version of record will be different from this version once it has been copyedited and typeset.
PLEASE CITE THIS ARTICLE AS DOI:10.1063/1.5123013

AIP Publishing

Dynamic Structure Factor of Correlated Electrons: From the Electron Liquid to Warm Dense Matter, *Phys. Rev. Lett.* **121**, 255001 (2018)

[19] M. Higuchi and H. Yasuhara, Kleinman's Dielectric Function and Interband Optical Absorption Strength of Simple Metals, *J. Phys. Soc. Jpn.* **69**, 2099–2106 (2000)

[20] S.H. Vosko, L. Wilk, and M. Nusair, Accurate Spin-Dependent Electron Liquid Correlation Energies for Local Spin Density Calculations: A Critical Analysis, *Can. J. Phys.* **58**, 1200 (1980)

[21] J.P. Perdew and A. Zunger, Self-interaction correction to density-functional approximations for many-electron systems, *Phys. Rev. B* **23**, 5048 (1981)

[22] J.P. Perdew and Y. Wang, Pair-distribution function and its coupling-constant average for the spin-polarized electron gas, *Phys. Rev. B* **46**, 12947 (1992)

[23] P. Gori-Giorgi, F. Sacchetti, and G.B. Bachelet, Analytic static structure factors and pair-correlation functions for the unpolarized homogeneous electron gas, *Phys. Rev. B* **61**, 7353 (2000)

[24] P. Gori-Giorgi and J.P. Perdew, Pair distribution function of the spin-polarized electron gas: A first-principles analytic model for all uniform densities, *Phys. Rev. B* **66**, 165118 (2002)

[25] T. Chachiyo, Communication: Simple and accurate uniform electron gas correlation energy for the full range of densities, *J. Chem. Phys.* **145**, 021101 (2016)

[26] D.M. Ceperley, Ground state of the fermion one-component plasma: A Monte Carlo study in two and three dimensions, *Phys. Rev. B.* **18**, 3126-3138 (1978)

[27] S. Moroni, D.M. Ceperley, and G. Senatore, Static Response and Local Field Factor of the Electron Gas, *Phys. Rev. Lett.* **75**, 689 (1995)

[28] G.G. Spink, R.J. Needs, and N.D. Drummond, Quantum Monte Carlo study of the three-dimensional spin-polarized homogeneous electron gas, *Phys. Rev. B* **88**, 085121 (2013)

[29] G. Ortiz and P. Ballone, Correlation energy, structure factor, radial distribution function, and momentum distribution of the spin-polarized uniform electron gas, *Phys. Rev. B* **50**, 1391 (1994)

[30] G. Ortiz, M. Harris, and P. Ballone, Zero Temperature Phases of the Electron Gas, *Phys. Rev. Lett.* **82**, 5317 (1999)

[31] R.O. Jones, Density functional theory: Its origins, rise to prominence, and future, *Rev. Mod. Phys.* **87**, 897 (2015)

[32] K. Burke, Perspective on density functional theory, *J. Chem. Phys.* **136**, 150901 (2012)

[33] We assume Hartree atomic units throughout this work.

[34] A.A. Kugler, Theory of the Local Field Correction in an Electron Gas, *J. Stat. Phys.* **12**, 35 (1975)

[35] We note that while the RPA provides a description of the density response of the system on a mean field level, it gives a nonvanishing correlation energy when inserted into the fluctuation dissipation theorem and the adiabatic connection formula (see, e.g., Ref. [98]), and approaches the exact limit for $r_s = 0$.

[36] J. Hubbard, The Description of Collective Motions in Terms of Many-Body Perturbation Theory, *Proc. Roy. Soc. (London) A* **243**, 336 (1957)

[37] D. Kraus, B. Bachmann, B. Barbrel, R.W. Falcone, L.B. Fletcher, S. Frydrych, E.J. Gamboa, M. Gauthier, D.O. Gericke, S.H. Glenzer, S. Göde, E.Granados, N.J. Hartley, J. Helfrich, H.J. Lee, B. Nagler, A. Ravasio, W. Schumaker, J. Vorberger, T. Döppner, Characterizing the Ionization Depression Potential Depression in Dense Carbon Plasmas with High-Precision Spectrally Resolved X-ray scattering, *Plasma Phys. Control. Fusion* **61**, 014015 (2018)

[38] K.-U. Plagemann, P. Sperling, R. Thiele, M.P. Desjarlais, C. Fortmann, T. Döppner, H.J. Lee, S.H. Glenzer, and R. Redmer, Dynamic structure factor in warm dense beryllium, *New J. Phys.* **14**, 055020 (2012)

[39] P. Neumayer, C. Fortmann, T. Döppner, P. Davis, R.W. Falcone, A.L. Kritcher, O.L. Landen, *et al.*, Plasmons in Strongly Coupled Shock-Compressed Matter, *Phys. Rev. Lett.* **105**, 075003 (2010)

[40] C. Fortmann, A. Wierling, and G. Röpke, Influence of Local-Field Corrections on Thomson Scattering in Collision-Dominated Two-Component Plasmas, *Phys. Rev. E* **81**, 026405 (2010)

[41] P. Neumayer, C. Fortmann, T. Döppner, P. Davis, R.W. Falcone, A.L. Kritcher, O.L. Landen, H.J. Lee, R.W. Lee, C. Niemann, S. Le Pape, and S.H. Glenzer, Plasmons in Strongly Coupled Shock-Compressed Matter, *Phys. Rev. Lett.* **105**, 075003 (2010)

[42] G. Senatore, S. Moroni, and D.M. Ceperley, Local field factor and effective potentials in liquid metals, *J. Non-Cryst. Sol.* **205-207**, 851-854 (1996)

[43] Zh.A. Moldabekov, S. Groth, T. Dornheim, H. Kählert, M. Bonitz, and T.S. Ramazanov, Structural characteristics of strongly coupled ions in a dense quantum plasma, *Phys. Rev. E* **98**, 023207 (2018)

[44] Zh.A. Moldabekov, H. Kählert, T. Dornheim, S. Groth, M. Bonitz, and T.S. Ramazanov, Dynamical structure factor of strongly coupled ions in a dense quantum plasma, *Phys. Rev. E* **99**, 053203 (2019)

[45] A. Pribram-Jones, P.E. Grabowski, and K. Burke, Thermal Density Functional Theory: Time-Dependent Linear Response and Approximate Functionals from the Fluctuation-Dissipation Theorem, *Phys. Rev. Lett.* **116**, 233001 (2016)

[46] D. Lu, Evaluation of model exchange-correlation kernels in the adiabatic connection fluctuation-dissipation theorem for inhomogeneous systems, *J. Chem. Phys.* **140**, 18A520 (2014)

[47] C.E. Patrick and K.S. Thygesen, Adiabatic-connection fluctuation-dissipation DFT for the structural properties of solids—The renormalized ALDA and electron gas kernels, *J. Chem. Phys.* **143**, 102802 (2015)

[48] A. Görling, Hierarchies of methods towards the exact Kohn-Sham correlation energy based on the adiabatic-connection fluctuation-dissipation theorem, *Phys. Rev. B* **99**, 235120 (2019)

[49] A. Diaw and M.S. Murillo, Generalized hydrodynamics model for strongly coupled plasmas, *Phys. Rev. E* **92**, 013107 (2015)

[50] A. Diaw and M.S. Murillo, A viscous quantum hydrodynamics model based on dynamic density functional theory, *Sci. Reports* **7**, 15352 (2017)

[51] Zh.A. Moldabekov, M. Bonitz, and T.S. Ramazanov, Theoretical foundations of quantum hydrodynamics for plasmas, *Phys. Plasmas* **25**, 031903 (2018)

[52] M.P. Desjarlais, P. Michael C.R. Scullard, L.X. Benedict, H.D. Whitley, and R. Redmer, Density-functional calculations of transport properties in the nondegenerate limit and the role of electron-electron scattering

The Journal of Chemical Physics
ACCEPTED MANUSCRIPT
This is the author's peer reviewed, accepted manuscript. However, the online version of record will be different from this version once it has been copyedited and typeset.
PLEASE CITE THIS ARTICLE AS DOI:10.1063/1.5123013
AIP Publishing

Phys. Rev. E **95**, 033203 (2017)

[53] M. Veysman, G. Röpke, M. Winkel, and H. Reinholz, Optical conductivity of warm dense matter within a wide frequency range using quantum statistical and kinetic approaches *Phys. Rev. E*, **94**, 013203 (2016)

[54] W. Cayzac, A. Frank, A. Ortner, V. Bagnoud, M.M. Basko, S. Bedacht, C. Bläser, A. Blazevic, S. Busold, O. Deppert, J. Ding, M. Ehret, P. Fiala, S. Frydrych, D.O. Gericke, L. Hallo, J. Helfrich, D. Jahn, E. Kjartansson, A. Knetsch, D. Kraus, G. Malka, N.W. Neumann, K. Pépitone, D. Pepler, S. Sander, G. Schaumann, T. Schlegel, N. Schroeter, D. Schumacher, M. Seibert, A. Tauschwitz, J. Vorberger, F. Wagner, S. Weih, Y. Zobus, and M. Roth, Experimental discrimination of ion stopping models near the Bragg peak in highly ionized matter, *Nature Comm.* **8**, 15693 (2017)

[55] Z.-G. Fu,Z. Wang, and P. Zhang, Energy loss of α-particle moving in warm dense deuterium plasma: Role of local field corrections, *Phys. Plasmas* **24**, 112710 (2017)

[56] J. Vorberger, D.O. Gericke, Th. Bornath, and M. Schlanges, Energy relaxation in dense, strongly coupled two-temperature plasmas, *Phys. Rev. E* **81**, 046404 (2010)

[57] S. Moroni, D.M. Ceperley, and G. Senatore, Static response from quantum Monte Carlo calculations, *Phys. Rev. Lett.* **69**, 1837 (1992)

[58] C. Bowen, G. Sugiyama, and B.J. Alder, Static Dielectric Response of the Electron Gas, *Phys. Rev. B* **50**, 14838 (1994)

[59] M. Corradini, R. Del Sole, G. Onida, and M. Palummo, Analytical Expressions for the Local-Field Factor $G(q)$ and the Exchange-Correlation Kernel $K_{\mathrm{xc}}(r)$ of the Homogeneous Electron Gas, *Phys. Rev. B* **57**, 14569 (1998)

[60] J. Vorberger, I. Tamblyn, B. Militzer, and S.A. Bonev, Hydrogen-helium mixtures in the interiors of giant planets, *Phys. Rev. B* **75**, 024206 (2007)

[61] M.D. Knudson, M.P. Desjarlais, R.W. Lemke, T.R. Mattsson, M. French, N. Nettelmann, and R. Redmer, Probing the Interiors of the Ice Giants: Shock Compression of Water to 700 GPa and 3.8 g/cm^3, *Phys. Rev. Lett.* **108**, 091102 (2012)

[62] F. Soubiran, B. Militzer, K.P. Driver, and S. Zhang, Properties of hydrogen, helium, and silicon dioxide mixtures in giant planet interiors, *Phys. Plasmas* **24**, 041401 (2017)

[63] M. Schöttler and R. Redmer, Ab Initio Calculation of the Miscibility Diagram for Hydrogen-Helium Mixtures, *Phys. Rev. Lett.* **120**, 115703 (2018)

[64] D. Saumon, W.B. Hubbard, G. Chabrier, and H.M. van Horn, The role of the molecular-metallic transition of hydrogen in the evolution of Jupiter, Saturn, and brown dwarfs, *Astrophys. J.* **391**, 827-831 (1992)

[65] W.B. Hubbard, T. Guillot, J.I. Lunine, A. Burrows, D. Saumon, M.S. Marley, and R. S. Freedman, Liquid metallic hydrogen and the structure of brown dwarfs and giant planets, *Phys. Plasmas* **4**, 2011–2015 (1997)

[66] A. Becker, W. Lorenzen, J.J. Fortney, N. Nettelmann, M. Schöttler, and R. Redmer, Ab initio equations of state for hydrogen (H-REOS.3) and helium (He-REOS.3) and their implications for the interior of brown dwarfs, *Astrophys. J. Suppl. Ser.* **215**, 21 (2014)

[67] M. Koenig *et al.*, Progress in the study of warm dense matter, *Plasma Phys. Control. Fusion* **47**, B441–B449 (2005)

[68] V.E. Fortov, Extreme states of matter on Earth and in space, *Phys.-Usp.* **52**, 615–647 (2009)

[69] K. Falk, Experimental methods for warm dense matter research, *High Power Laser Sci. Eng.* **6**, e59 (2018)

[70] R. Ernstorfer, M. Harb, C.T. Hebeisen, G. Sciaini, T. Dartigalongue, and R.J.D. Miller, The formation of warm dense matter: Experimental evidence for electronic bond hardening in gold, *Science* **323**, 1033 (2009)

[71] L. Waldecker, R. Bertoni, R. Ernstorfer, and J. Vorberger, Electron-Phonon Coupling and Energy Flow in a Simple Metal beyond the Two-Temperature Approximation, *Phys. Rev. X* **6**, 021003 (2016)

[72] A. Jayaraman, Diamond anvil cell and high-pressure physical investigations, *Rev. Mod. Phys.* **55**, 65 (1983)

[73] S. Mukherjee, F. Libisch, N. Large, O. Neumann, L.V. Brown, J. Cheng, J. Britt Lassiter, E.A. Carter, P. Nordlander, and N.J. Halas, Hot Electrons Do the Impossible: Plasmon-Induced Dissociation of H_2 on Au, *Nano Lett.* **13**, 240-247 (2013)

[74] M.L. Brongersma, N.J. Halas, and P. Nordlander, Plasmon-induced hot carrier science and technology, *Nat. Nanotechnol.* **10**, 25 (2015)

[75] S.X. Hu, B. Militzer, V.N. Goncharov, and S. Skupsky, *Phys. Rev. B* **84**, 224109 (2011)

[76] A.L. Kritcher, T. Döppner, C. Fortmann, T. Ma, O.L. Landen, R. Wallace, and S.H. Glenzer, In-Flight Measurements of Capsule Shell Adiabats in Laser-Driven Implosions, *Phys. Rev. Lett.* **107**, 015002 (2011)

[77] E. Zarkadoula, S.L. Daraszewicz, D.M. Duffy, M.A. Seaton, I.T. Todorov, K. Nordlund, M.T. Dove, and K. Trachenko, Electronic effects in high-energy radiation damage in iron, *J. Phys. Condens. Matter* **26**, 085401 (2014)

[78] F. Graziani, M.P. Desjarlais, R. Redmer, and S.B. Trickey (eds.), Frontiers and Challenges in Warm Dense Matter, Springer International Publishing (2014)

[79] N.D. Mermin, Thermal Properties of the Inhomogeneous Electron Gas, *Phys. Rev.* **137**, A1441 (1965)

[80] U. Gupta and A.K. Rajagopal, Density functional formalism at finite temperatures with some applications, *Phys. Reports* **87**, 259-311 (1982)

[81] E.W. Brown, B.K. Clark, J.L. DuBois, and D.M. Ceperley, Path-Integral Monte Carlo Simulation of the Warm Dense Homogeneous Electron Gas, *Phys. Rev. Lett.* **110**, 146405 (2013)

[82] T. Schoof, S. Groth, J. Vorberger, and M. Bonitz, Ab Initio Thermodynamic Results for the Degenerate Electron Gas at Finite Temperature, *Phys. Rev. Lett.* **115**, 130402 (2015)

[83] B. Militzer and K.P. Driver, Development of Path Integral Monte Carlo Simulations with Localized Nodal Surfaces for Second-Row Elements, *Phys. Rev. Lett.* **115**, 176403 (2015)

[84] T. Dornheim, S. Groth, A. Filinov and M. Bonitz, Permutation blocking path integral Monte Carlo: a highly efficient approach to the simulation of strongly degenerate non-ideal fermions, *New J. Phys.* **17**, 073017 (2015)

[85] F.D. Malone, N.S. Blunt, J.J. Shepherd, D.K.K. Lee, J.S. Spencer, and W.M.C. Foulkes, Interaction picture density matrix quantum Monte Carlo, *J. Chem. Phys.* **143**, 044116 (2015)

[86] T. Dornheim, T. Schoof, S. Groth, A. Filinov, and

The Journal of Chemical Physics

ACCEPTED MANUSCRIPT

This is the author's peer reviewed, accepted manuscript. However, the online version of record will be different from this version once it has been copyedited and typeset.

PLEASE CITE THIS ARTICLE AS DOI:10.1063/1.5123013

AIP Publishing

M. Bonitz, Permutation Blocking Path Integral Monte Carlo Approach to the Uniform Electron Gas at Finite Temperature, *J. Chem. Phys.* **143**, 204101 (2015)

[87] S. Groth, T. Schoof, T. Dornheim, and M. Bonitz, *Ab Initio* Quantum Monte Carlo Simulations of the Uniform Electron Gas without Fixed Nodes, *Phys. Rev. B* **93**, 085102 (2016)

[88] T. Dornheim, S. Groth, T. Schoof, C. Hann, and M. Bonitz, *Ab initio* quantum Monte Carlo simulations of the Uniform electron gas without fixed nodes: The unpolarized case, *Phys. Rev. B* **93**, 205134 (2016)

[89] T. Dornheim, S. Groth, T. Sjostrom, F.D. Malone, W.M.C. Foulkes, and M. Bonitz, *Ab Initio* Quantum Monte Carlo Simulation of the Warm Dense Electron Gas in the Thermodynamic Limit, *Phys. Rev. Lett.* **117**, 156403 (2016)

[90] F.D. Malone, N.S. Blunt, E.W. Brown, D.K.K. Lee, J.S. Spencer, W.M.C. Foulkes, and J.J. Shepherd, Accurate Exchange-Correlation Energies for the Warm Dense Electron Gas, *Phys. Rev. Lett.* **117**, 115701 (2016)

[91] J.L. DuBois, E.W. Brown, and B.J. Alder, Overcoming the Fermion Sign Problem in Homogeneous Systems, in E. Schwegler, B.M. Rubenstein, and S.B. Libby (Eds.), Advances in the Computational Sciences-Symposium in Honor of Dr Berni Alder's 90th Birthday, World Scientific, Singapore (2017)

[92] T. Dornheim, S. Groth, J. Vorberger, and M. Bonitz, Permutation Blocking Path Integral Monte Carlo approach to the Static Density Response of the Warm Dense Electron Gas, *Phys. Rev. E* **96**, 023203 (2017)

[93] T. Dornheim, S. Groth, and M. Bonitz, Ab initio results for the Static Structure Factor of the Warm Dense Electron Gas, *Contrib. Plasma Phys.* **57**, 468-478 (2017)

[94] T. Dornheim, S. Groth, and M. Bonitz, Permutation Blocking Path Integral Monte Carlo Simulations of Degenerate Electrons at Finite Temperature, *Contrib. Plasma Phys.* **59**, e201800157 (2019)

[95] T. Dornheim, S. Groth, F.D. Malone, T. Schoof, T. Sjostrom, W.M.C. Foulkes, and M. Bonitz, *Ab Initio* Quantum Monte Carlo Simulation of the Warm Dense Electron Gas, *Phys. Plasmas* **24**, 056303 (2017)

[96] S. Groth, T. Dornheim, T. Sjostrom, F.D. Malone, W.M.C. Foulkes, and M. Bonitz, *Ab initio* Exchange–Correlation Free Energy of the Uniform Electron Gas at Warm Dense Matter Conditions, *Phys. Rev. Lett.* **119**, 135001 (2017)

[97] V.V. Karasiev, T. Sjostrom, J.W. Dufty, and S.B. Trickey, Accurate Homogeneous Electron Gas Exchange-Correlation Free Energy for Local Spin-Density Calculations, *Phys. Rev. Lett.* **112**, 076403 (2014)

[98] T. Dornheim, S. Groth, and M. Bonitz, The uniform electron gas at warm dense matter conditions, *Phys. Reports* **744**, 1–86 (2018)

[99] M.G. Medvedev, I.S. Bushmarinov, J. Sun, J.P. Perdew, and K.A. Lyssenko, Density functional theory is straying from the path toward the exact functional, *Science* **355**, 49-52 (2017)

[100] A. Pribram-Jones, D.A. Gross, and K. Burke, DFT: A Theory Full of Holes?, *Ann. Rev. Phys. Chem.* **66**, 283-304 (2015)

[101] S. Tanaka and S. Ichimaru, Thermodynamics and Correlational Properties of Finite-Temperature Electron Liquids in the Singwi-Tosi-Land-Sjölander Approximation, *J. Phys. Soc. Jpn.* **55**, 2278-2289 (1986)

[102] T. Sjostrom, and J. Dufty, Uniform Electron Gas at Finite Temperatures, *Phys. Rev. B* **88**, 115123 (2013)

[103] S. Tanaka, Correlational and thermodynamic properties of finite-temperature electron liquids in the hypernetted-chain approximation, *J. Chem. Phys.* **145**, 214104 (2016)

[104] S. Groth, T. Dornheim, and J. Vorberger, *Ab initio* path integral Monte Carlo approach to the static and dynamic density response of the uniform electron gas, *Phys. Rev. B* **99**, 235122 (2019)

[105] T. Dornheim, The Fermion Sign Problem in Path Integral Monte Carlo Simulations: Quantum Dots, Ultracold Atoms, and Warm Dense Matter, *Phys. Rev. E* **100**, 023307 (2019)

[106] M. Troyer and U.J. Wiese, Computational Complexity and Fundamental Limitations to Fermionic Quantum Monte Carlo Simulations, *Phys. Rev. Lett.* **94**, 170201 (2005)

[107] S. Groth, T. Dornheim, and M. Bonitz, Configuration Path Integral Monte Carlo approach to the Static Density Response of the Warm Dense Electron Gas, *J. Chem. Phys.* **147**, 164108 (2017)

[108] We have used the Keras [109] frontend on the basis of TensorFlow [110].

[109] F. Chollet *et al.*, Keras, keras.io (2015)

[110] Martín Abadi, Ashish Agarwal, Paul Barham, Eugene Brevdo, Zhifeng Chen, Craig Citro, Greg S. Corrado, Andy Davis, Jeffrey Dean, Matthieu Devin, Sanjay Ghemawat, Ian Goodfellow, Andrew Harp, Geoffrey Irving, Michael Isard, Yangqing Jia, Rafal Jozefowicz, Lukasz Kaiser, Manjunath Kudlur, Josh Levenberg, Dandelion Mané, Rajat Monga, Sherry Moore, Derek Murray, Chris Olah, Mike Schuster, Jonathon Shlens, Benoit Steiner, Ilya Sutskever, Kunal Talwar, Paul Tucker, Vincent Vanhoucke, Vijay Vasudevan, Fernanda Viégas, Oriol Vinyals, Pete Warden, Martin Wattenberg, Martin Wicke, Yuan Yu and Xiaoqiang Zheng, TensorFlow: Large-Scale Machine Learning on Heterogeneous Systems, Software available from tensorflow.org (2015)

[111] A link to both the ML representation of the static LFC and the PIMC raw data for the density response will be provided upon publication.

[112] P. Arora, K. Kumar, and R.K. Moudgil, Spin-resolved correlations in the warm-dense homogeneous electron gas, *Eur. Phys. J. B* **90**, 76 (2017)

[113] M. Panholzer, R. Hobbiger, and H. Böhm, Optimized correlations inspired by perturbation theory, *Phys. Rev. B* **99**, 195156 (2019)

[114] F. Mezzacapo and M. Boninsegni, Superfluidity and Quantum Melting of $p-\mathrm{H}_2$ Clusters, *Phys. Rev. Lett.* **97**, 045301 (2006)

[115] F. Mezzacapo and M. Boninsegni, Structure, superfluidity, and quantum melting of hydrogen clusters, *Phys. Rev. A* **75**, 033201 (2007)

[116] M. Boninsegni, N.V. Prokofev, and B.V. Svistunov, Worm algorithm and diagrammatic Monte Carlo: A new approach to continuous-space path integral Monte Carlo simulations, *Phys. Rev. E* **74**, 036701 (2006)

[117] M. Boninsegni, N.V. Prokofev, and B.V. Svistunov, Worm Algorithm for Continuous-Space Path Integral Monte Carlo Simulations, *Phys. Rev. Lett.* **96**, 070601 (2006)

ACCEPTED MANUSCRIPT
The Journal of Chemical Physics
AIP Publishing
This is the author's peer reviewed, accepted manuscript. However, the online version of record will be different from this version once it has been copyedited and typeset.
PLEASE CITE THIS ARTICLE AS DOI:10.1063/1.5123013

[118] D.M. Ceperley, Path integrals in the theory of condensed helium, *Rev. Mod. Phys.* **67**, 279-355 (1995)

[119] D.M. Ceperley, Fermion nodes, *J. Stat. Phys.* **63**, 1237-1267 (1991)

[120] G. Sugiyama, C. Bowen, and B.J. Alder, Static dielectric response of charged bosons, *Phys. Rev. B* **46**, 13042 (1992)

[121] A. Filinov, N.V. Prokof'ev, and M. Bonitz, Berezinskii-Kosterlitz-Thouless Transition in Two-Dimensional Dipole Systems, *Phys. Rev. Lett.* **105**, 070401 (2010)

[122] A.A. Kugler, Bounds for Some Equilibrium Properties of an Electron Gas, *Phys. Rev. A* **1**, 1688 (1970)

[123] A. Holas, Exact asymptotic expression for the static dielectric function of a uniform electron liquid at large wave vector, in Strongly Coupled Plasma Physics, edited by F.J. Rogers and H.E. DeWitt (Plenum,NewYork,1987), p.46

[124] This is, among other things, due to the softening of the Fermi surface at finite temperature, and will be discussed in a separate publication.

[125] For completeness, we note that the inclusion of the exact large-q limit at finite temperature is not expected to improve the quality of our representation is the specified range of validity ($0 < q < 5q_\mathrm{F}$), but would potentially allow to extend it to $q \to \infty$.

[126] B. Farid, V. Heine, G.E. Engel, and I.J. Robertson, Extremal Properties of the Harris-Foulkes Functional and an Improved Screening Calculation for the Electron Gas, *Phys. Rev. B* **48**, 11602 (1993)

[127] B. Militzer and E.L. Pollock, Lowering of the kinetic energy in interacting quantum systems, *Phys. Rev. Lett.* **89**, 280401 (2002)

[128] W.D. Kraeft, M. Schlanges, J. Vorberger, and H.E. DeWitt, Kinetic and correlation energies and distribution functions of dense plasmas, *Phys. Rev. E* **66**, 046405 (2002)

[129] K. Hornik, M. Stinchcombe, and H. White, Multilayer feedforward networks are universal approximators, *Neural Networks* **2**, 359-366 (1989)

[130] D. Rolnick and M. Tegmark, The power of deeper networks for expressing natural functions, *International Conference on Learning Representations (ICLR)*, arxiv:1705.05502 (2018)

[131] S.H. Glenzer and R. Redmer, X-ray Thomson scattering in high energy density plasmas, *Rev. Mod. Phys.* **81**, 1625 (2009)

[132] A.D. Baczewski, L. Shulenburger, M.P. Desjarlais, S.B. Hansen, and R.J. Magyar, X-ray Thomson Scattering in Warm Dense Matter without the Chihara Decomposition, *Phys. Rev. Lett.* **116**, 115004 (2016)

[133] D. Kingma and J. Ba, Adam: A Method for Stochastic Optimization, *International Conference on Learning Representations (ICLR)*, arxiv:1412.6980v8 (2015)

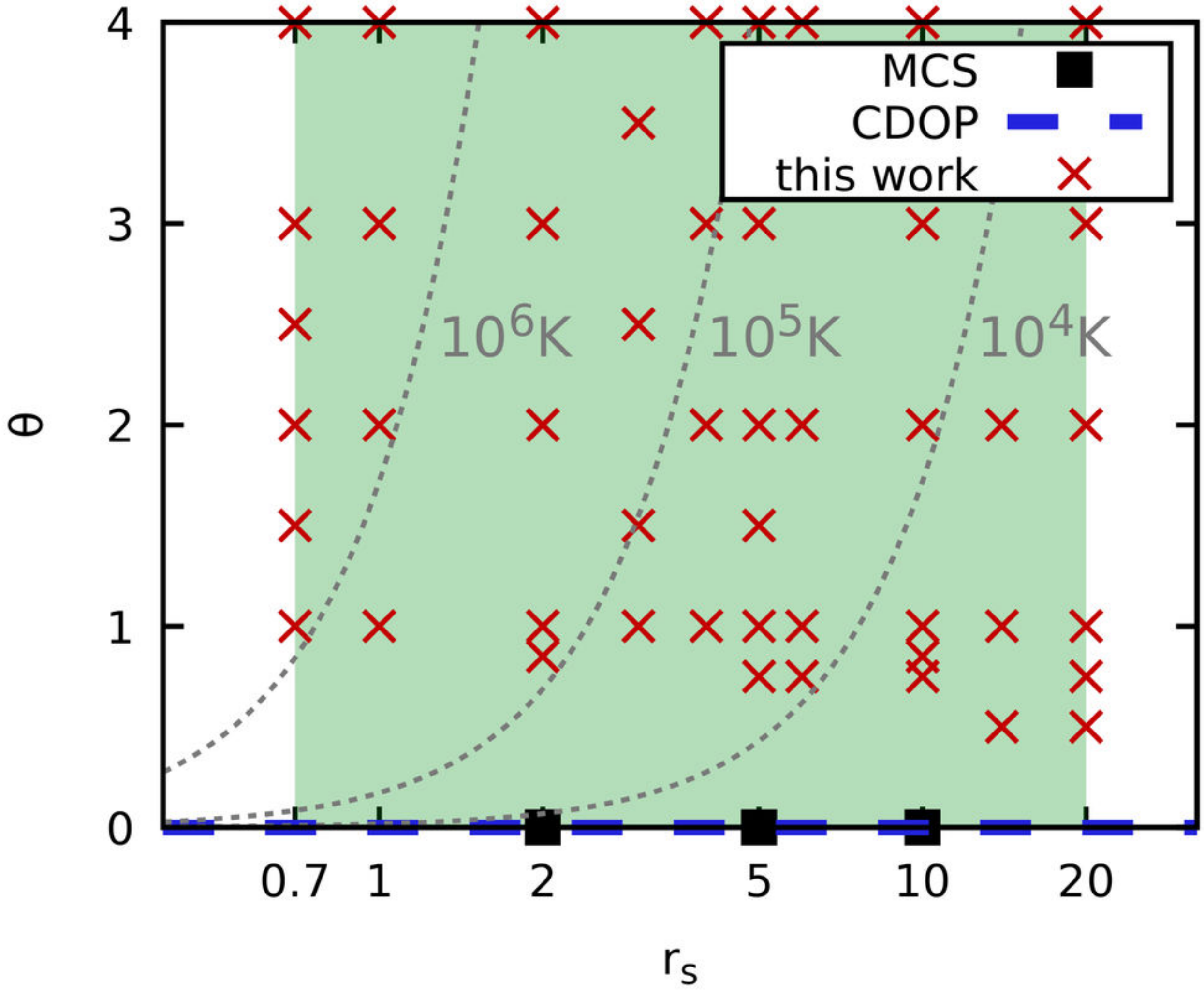
MCS
CDOP
this work
θ
r_s
4
3
2
1
0
0.7
1
2
5
10
20
10^6K
10^5K
10^4K

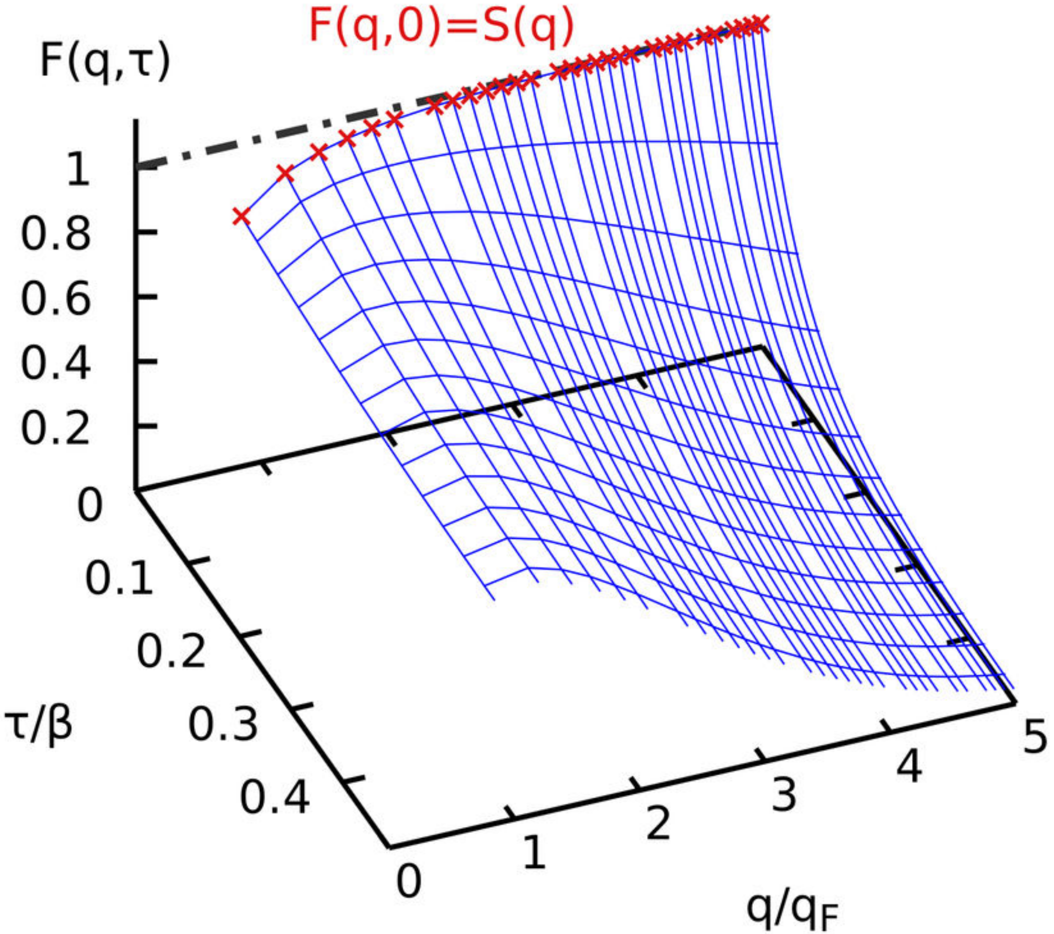
F(q,0)=S(q)
F(q,τ)
1
0.8
0.6
0.4
0.2
0
0.1
0.2
τ/β
0.3
0.4
0
1
2
3
4
5
q/q_F

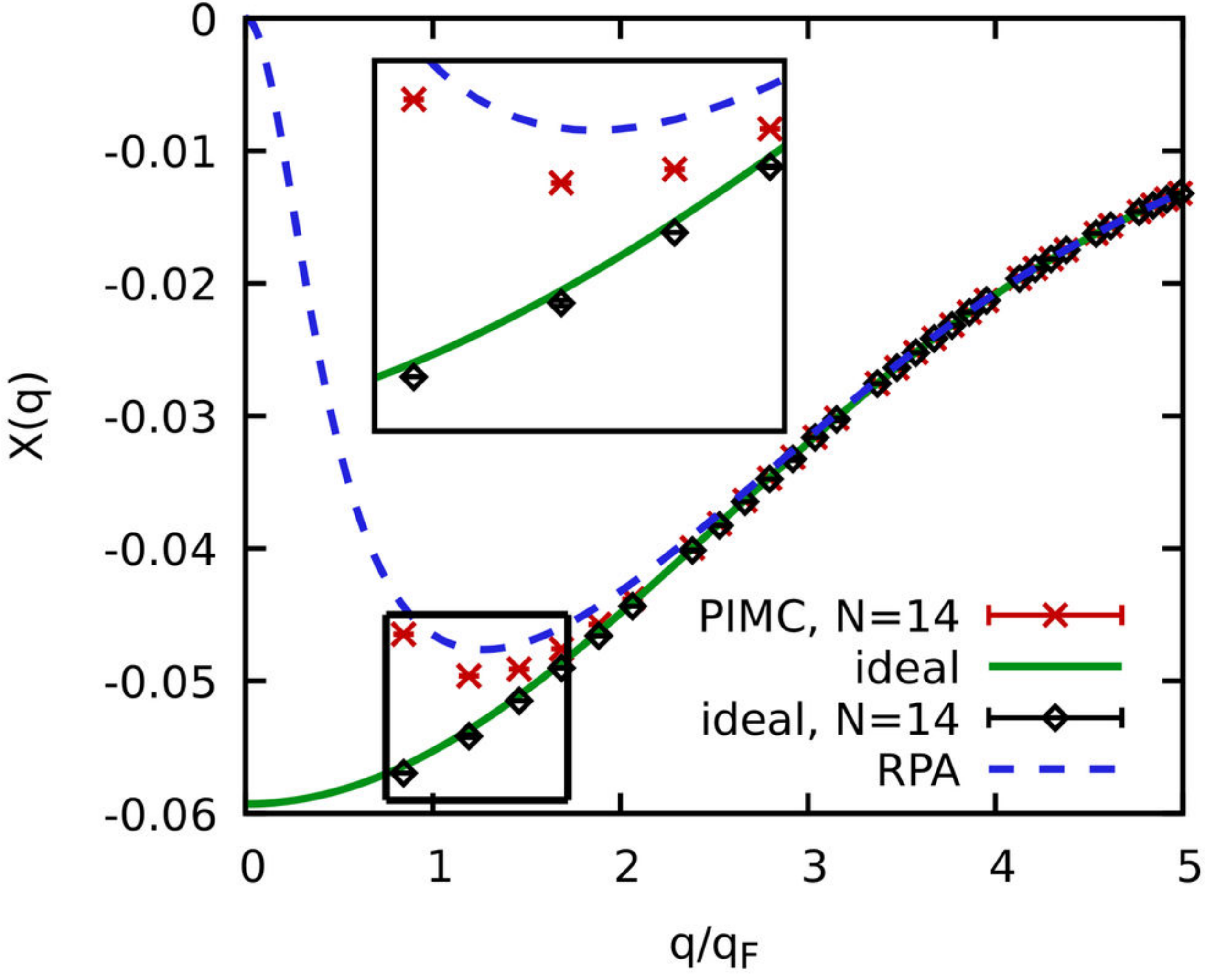
X(q)
0
-0.01
-0.02
-0.03
-0.04
-0.05
-0.06
0
1
2
3
4
5
q/q_F
PIMC, N=14
ideal
ideal, N=14
RPA

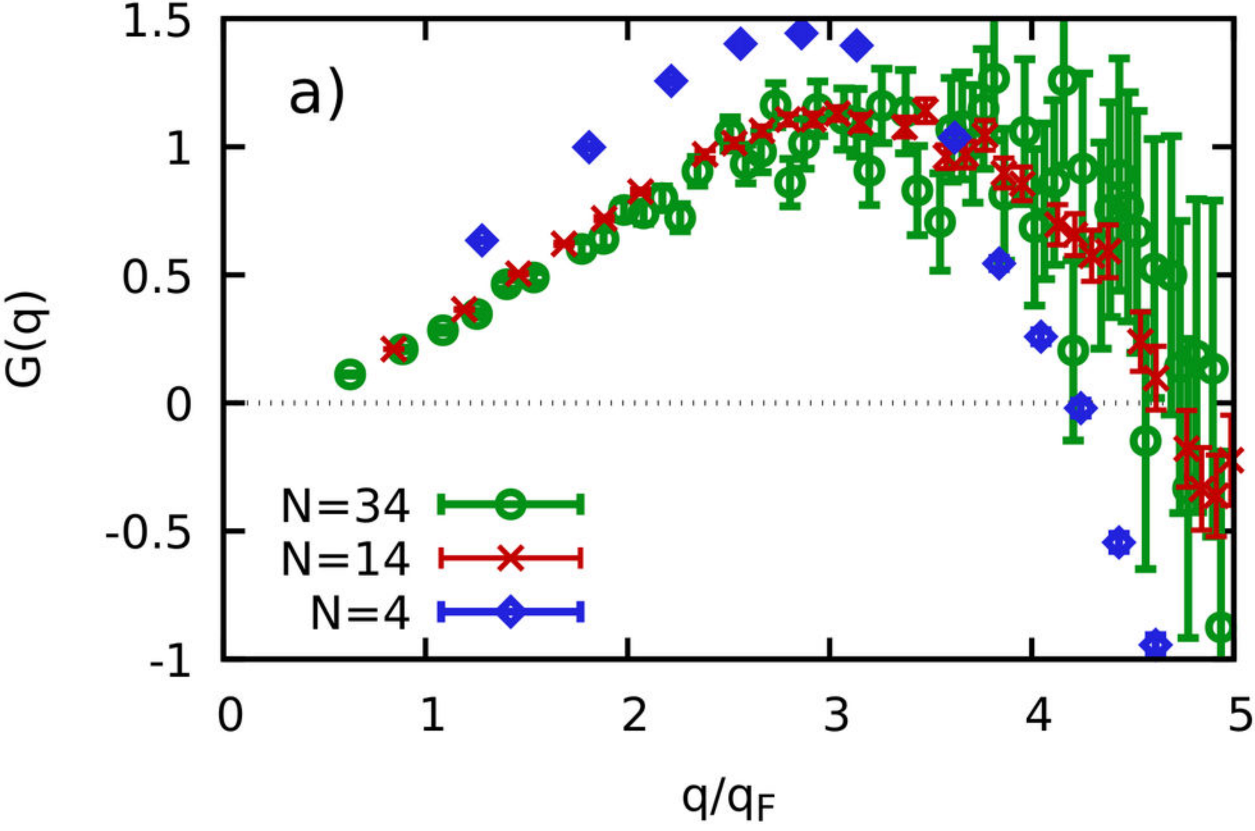
a)
G(q)
q/q_F
1.5
1
0.5
0
-0.5
-1
0
1
2
3
4
5
N=34
N=14
N=4

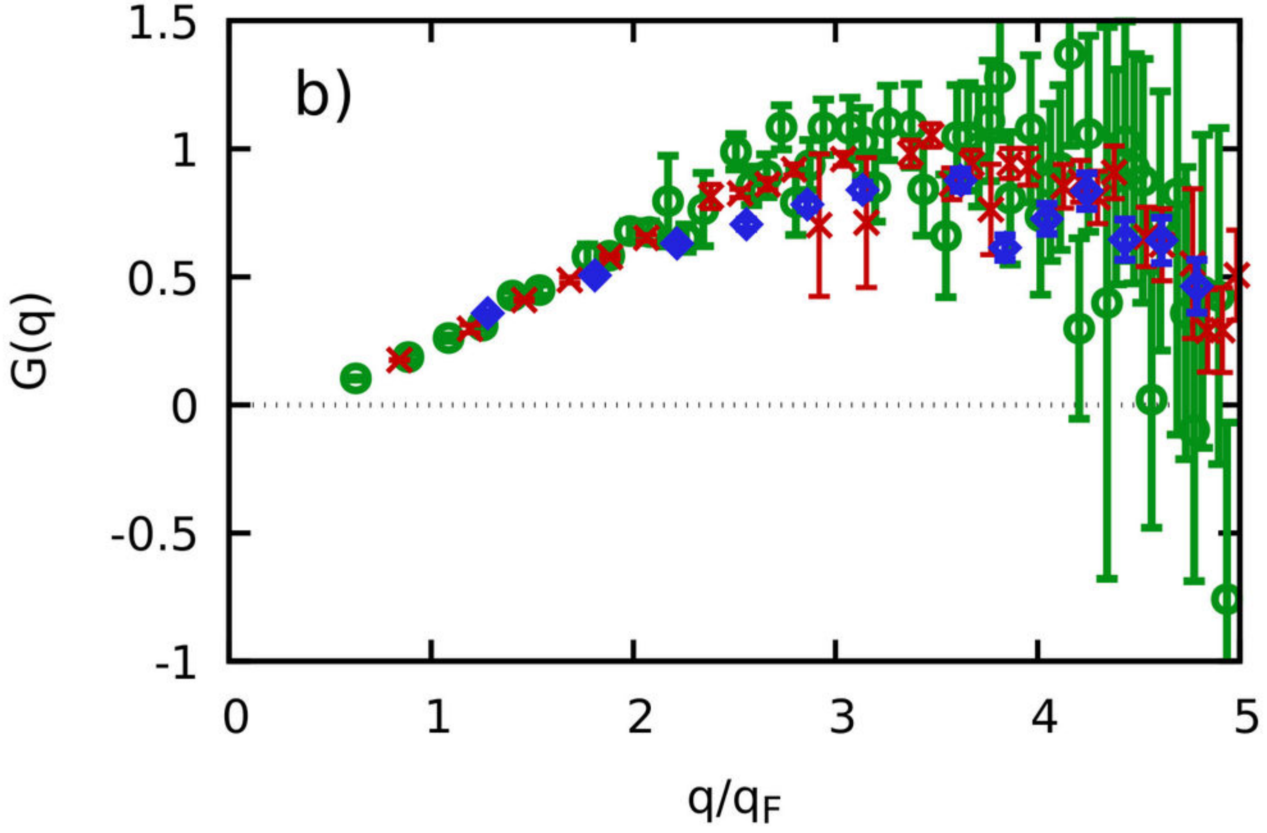
b)
G(q)
q/q_F
1.5
1
0.5
0
-0.5
-1
0
1
2
3
4
5

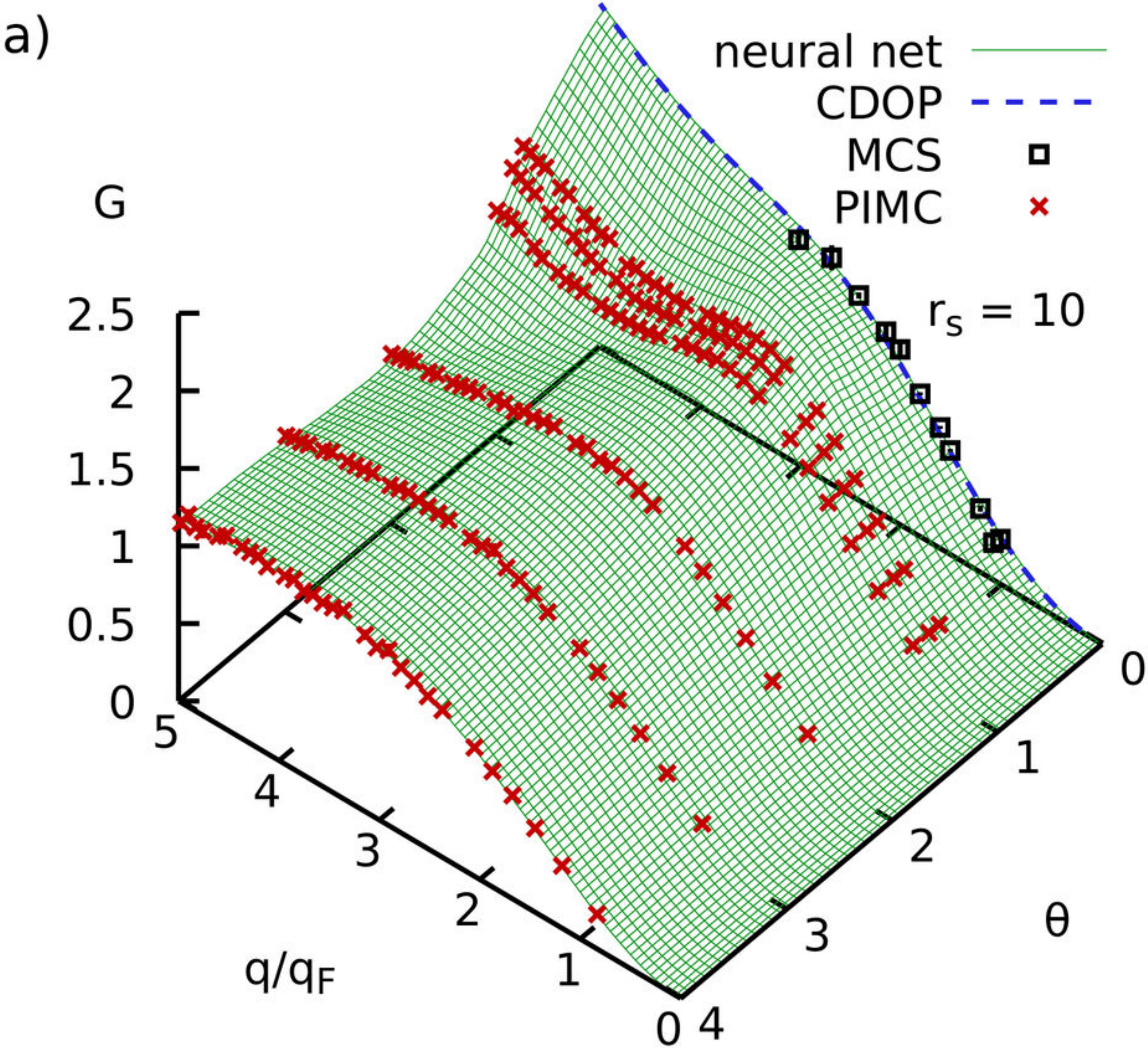

a)
neural net
CDOP
MCS
PIMC
G
2.5
2
1.5
1
0.5
0
$r_s = 10$
5
4
3
2
1
0
q/q_F
0
1
2
3
4
θ

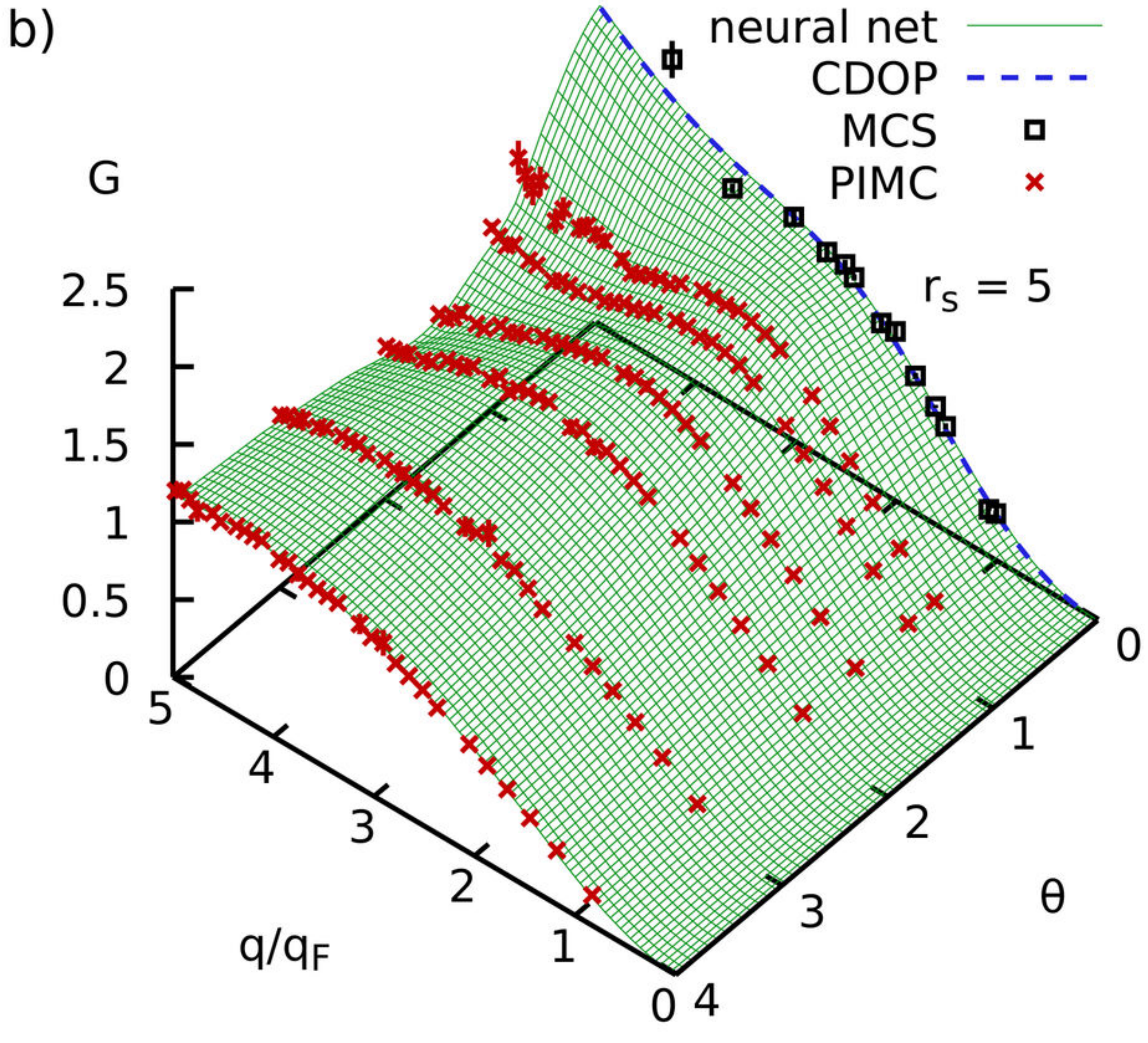
b)
neural net
CDOP
MCS
PIMC
G
$r_s = 5$
2.5
2
1.5
1
0.5
0
5
4
3
2
1
0
q/q_F
0
1
2
3
4
θ

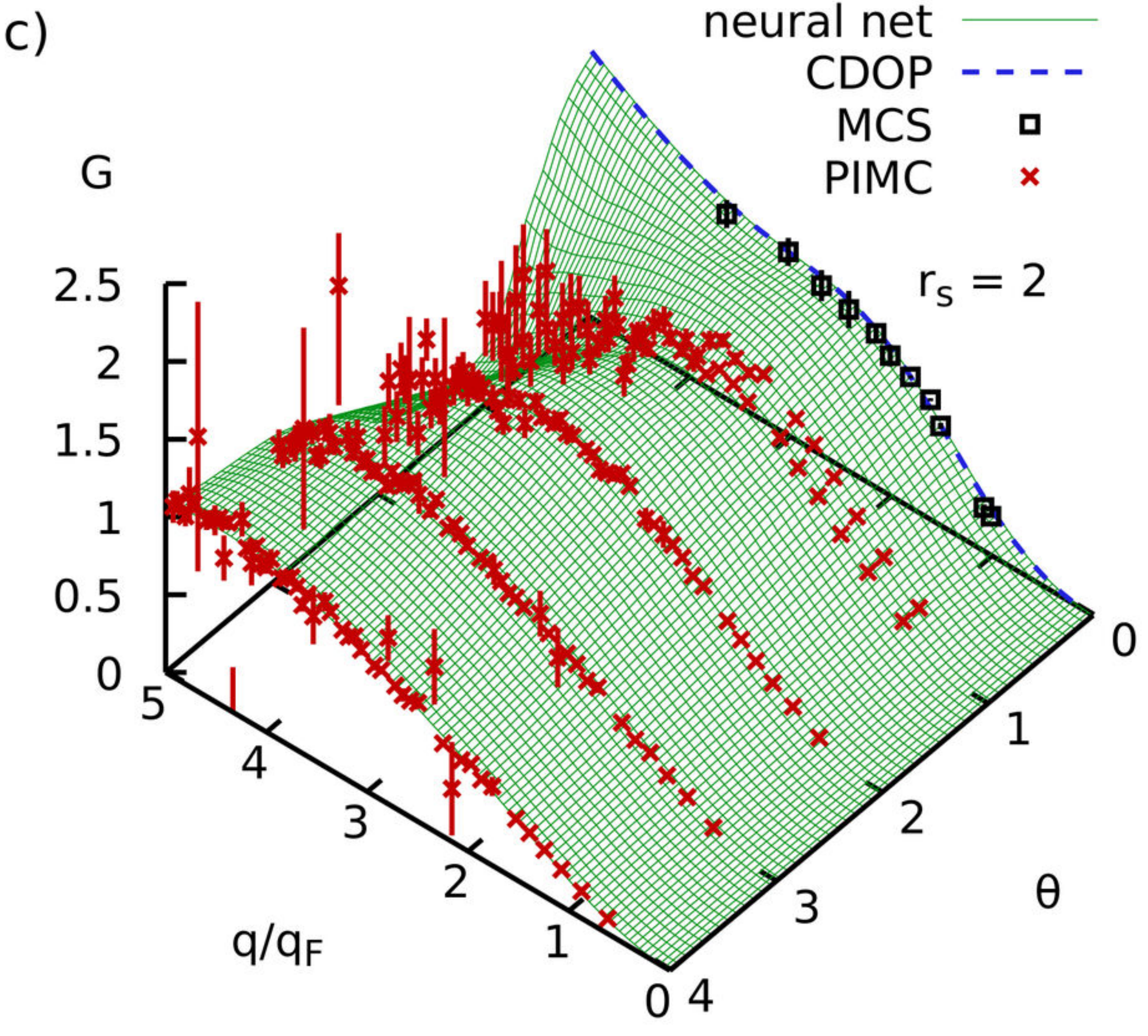
c)
neural net
CDOP
MCS
PIMC
G
$r_s = 2$
2.5
2
1.5
1
0.5
0
5
4
3
2
1
0
q/q_F
0
1
2
3
4
θ

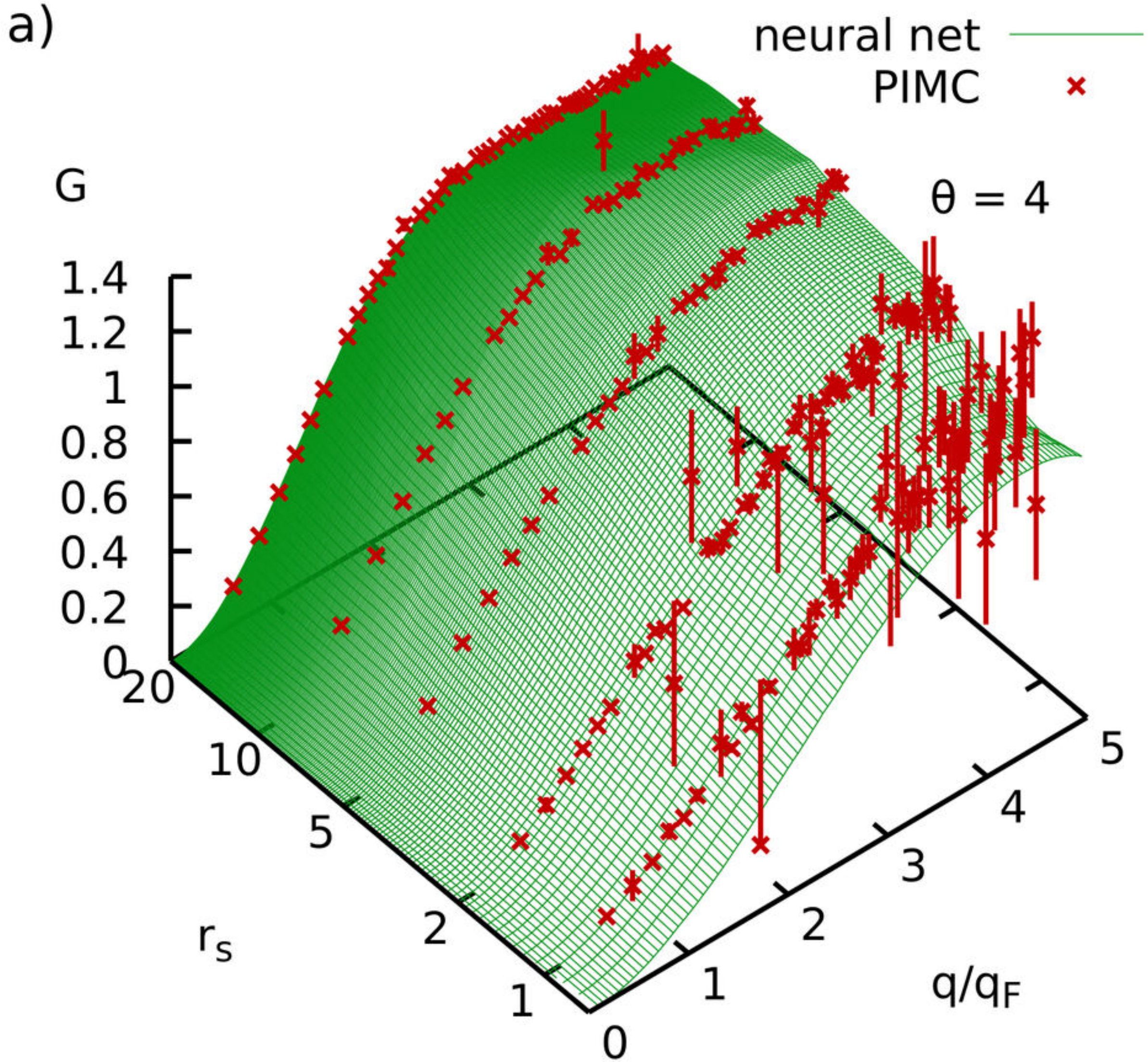
a)
neural net
PIMC
G
θ = 4
1.4
1.2
1
0.8
0.6
0.4
0.2
0
20
10
5
2
1
r_s
0
1
2
3
4
5
q/q_F

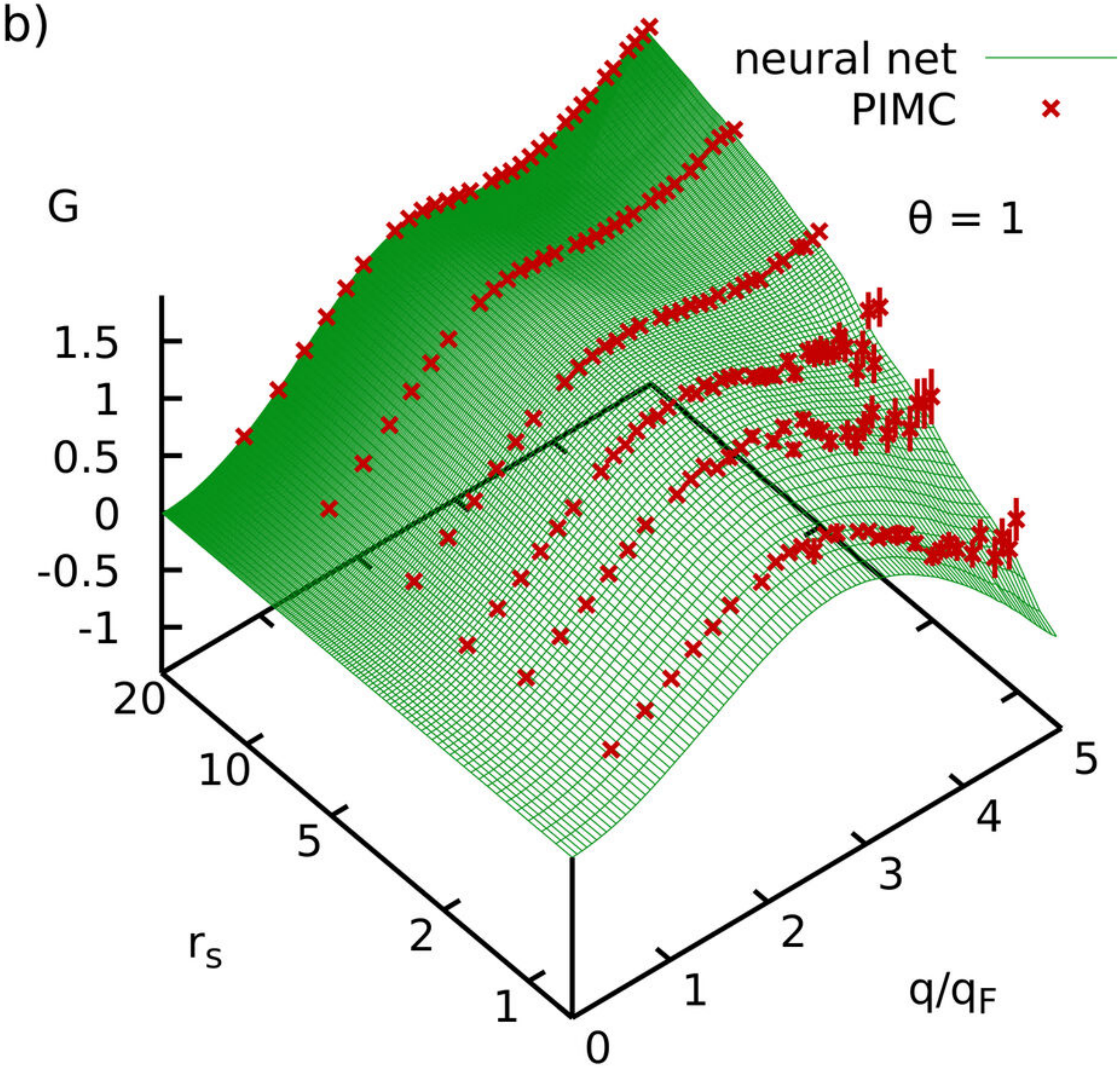
b)
neural net
PIMC
G
θ = 1
1.5
1
0.5
0
-0.5
-1
20
10
5
2
1
r_s
0
1
2
3
4
5
q/q_F

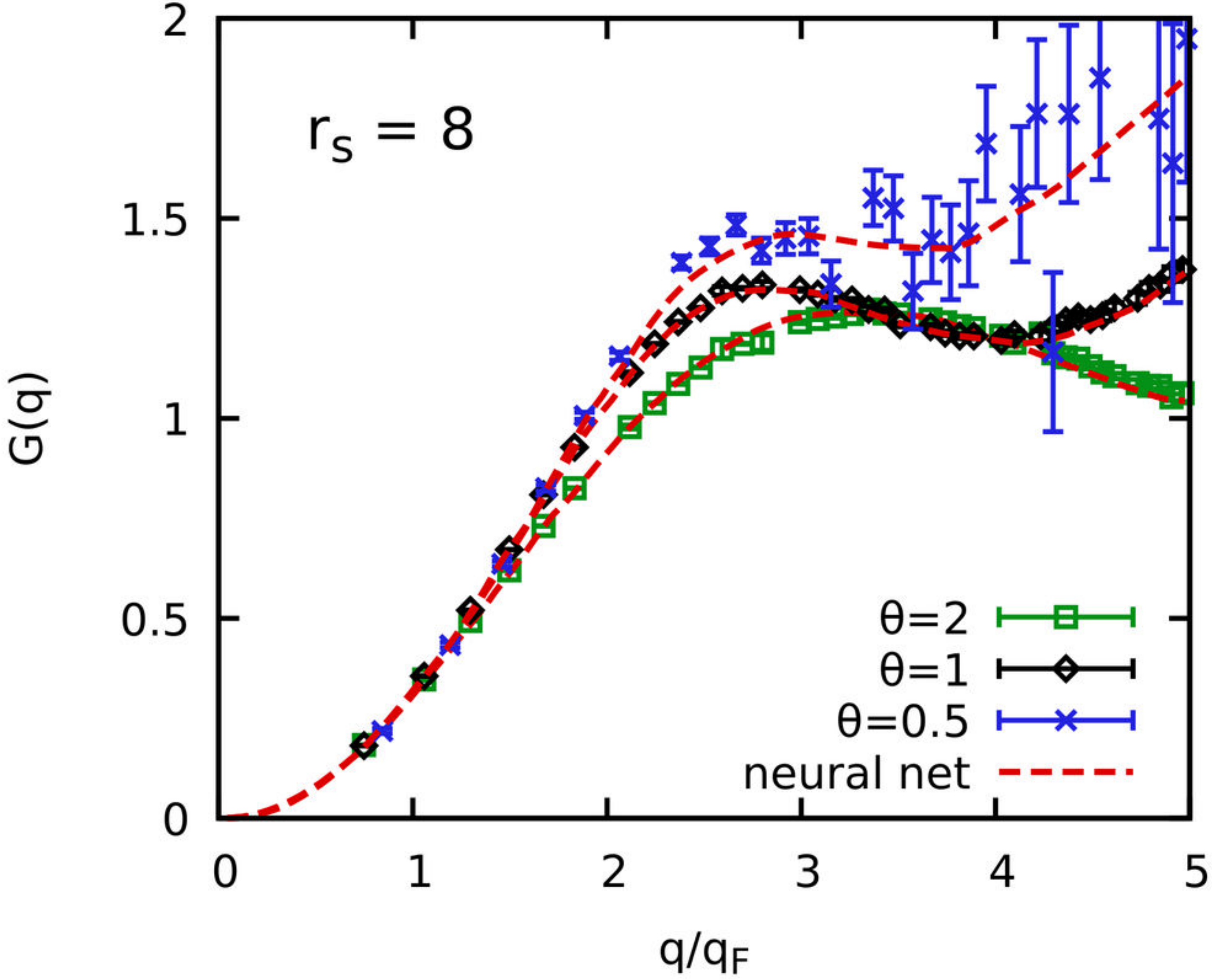
$r_s = 8$
G(q)
q/q_F
0
0.5
1
1.5
2
0
1
2
3
4
5
θ=2
θ=1
θ=0.5
neural net

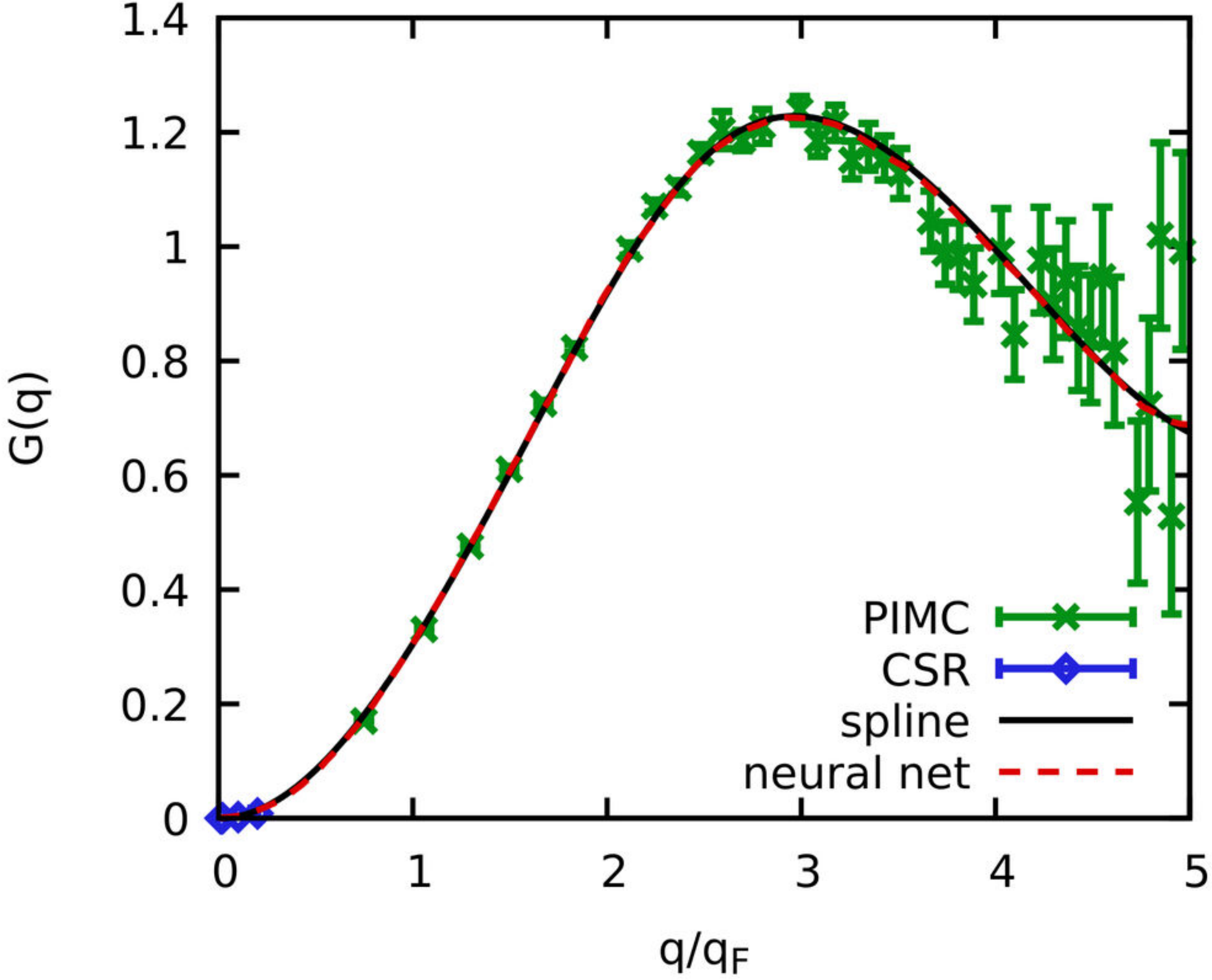
1.4
1.2
1
0.8
0.6
0.4
0.2
0
0
1
2
3
4
5
G(q)
q/q_F
PIMC
CSR
spline
neural net

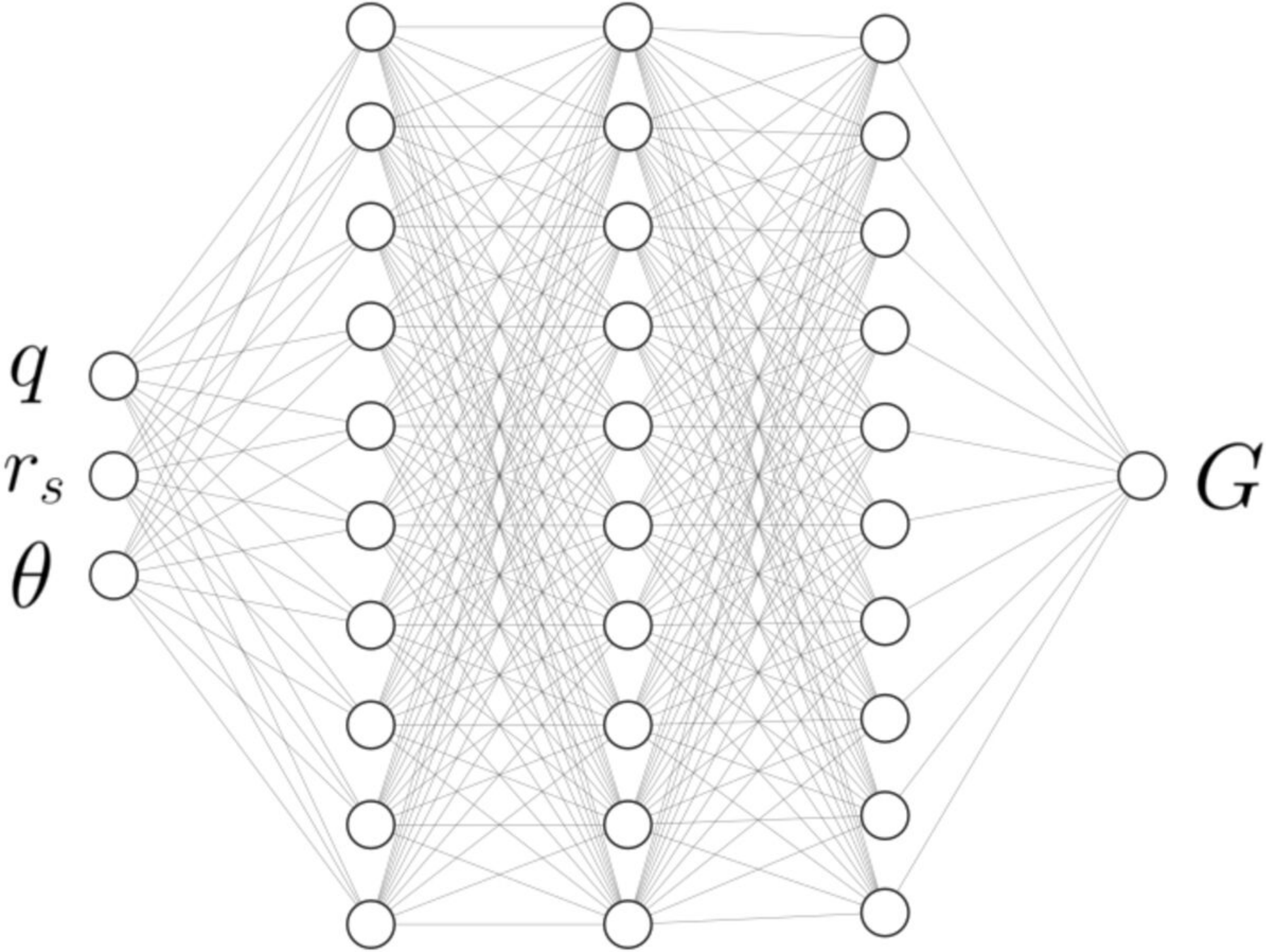
q
r_s
θ
G

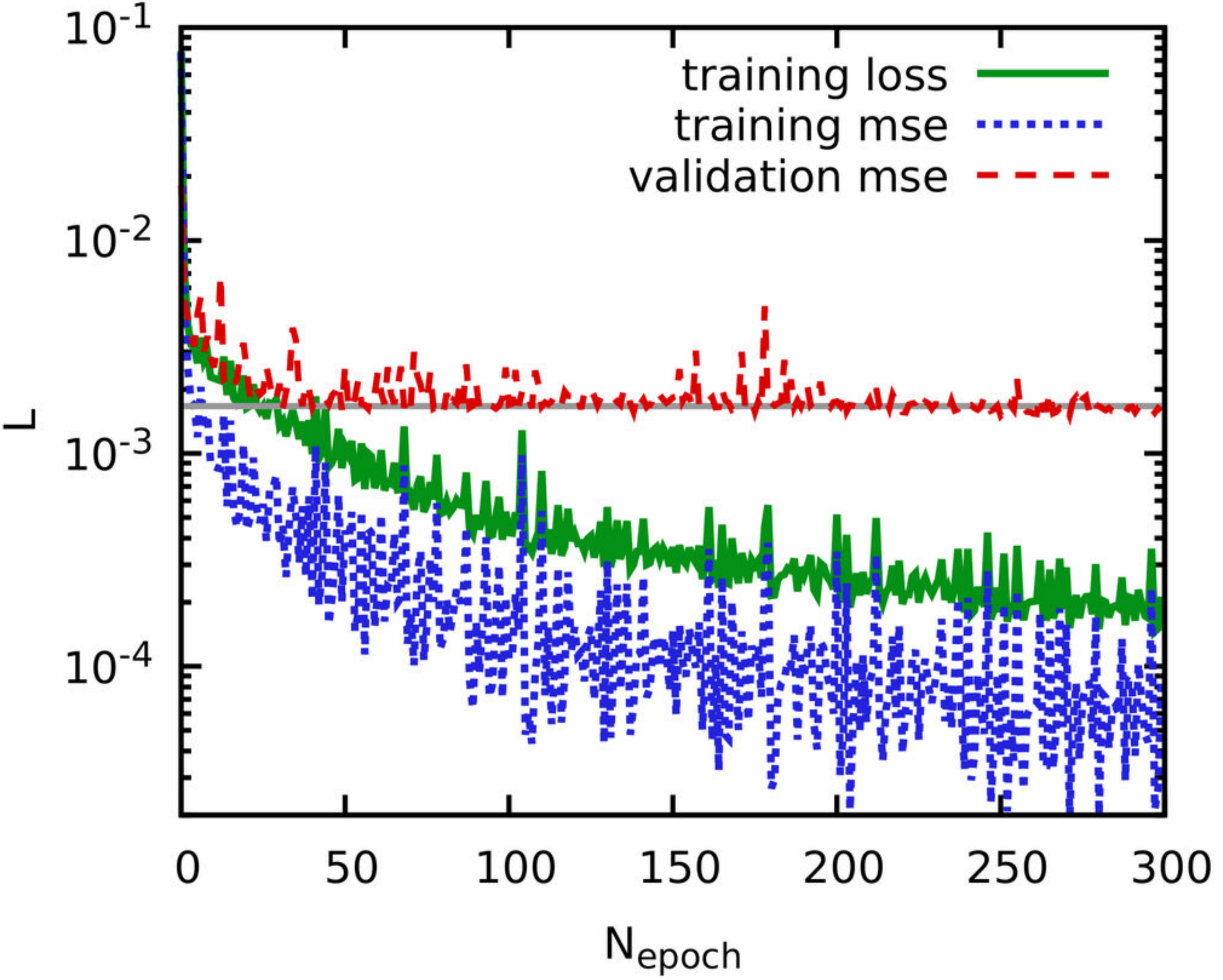
10-1
10-2
10-3
10-4
L
0
50
100
150
200
250
300
Nepoch
training loss
training mse
validation mse

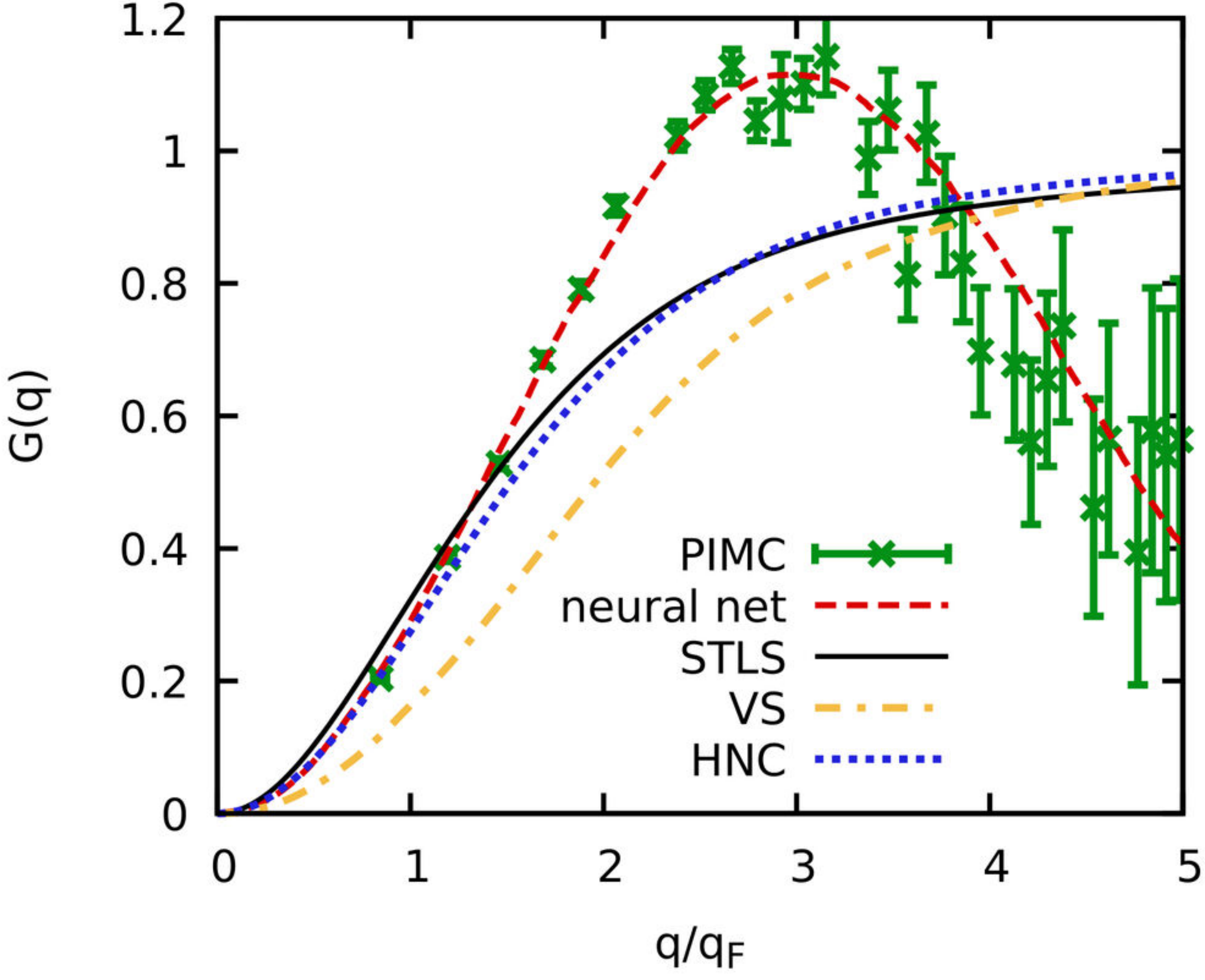
G(q)
1.2
1
0.8
0.6
0.4
0.2
0
0
1
2
3
4
5
q/q$_F$
PIMC
neural net
STLS
VS
HNC